



**Evaluation of tradewind cloud properties
using a passive
airborne microwave radiometer
during the NARVAL campaign**

Master's Thesis

submitted by
Sabrina Schnitt

Department of Physics
University of Cologne
21.12.2015

edited 02.05.2016

consultant: Prof. Dr. S. Crewell
2nd consultant: Prof. Dr. S. Schlemmer

Abstract

The representation of clouds in climate and weather models is associated with large uncertainties. Over the oceans and remote areas, satellite remote sensing applications provide continuous measurements of **I**ntegrated **W**ater **V**apor (IWV) and cloud macrophysical properties such as the **L**iquid **W**ater **P**ath (LWP). Evaluation of the spaceborne applications can be performed by finely resolved airborne measurements. During the **N**ext **G**eneration **A**ircraft **R**emote-sensing for **V**ALidation studies (NARVAL)-South campaign in December 2013, shallow cumulus clouds over the Atlantic were observed with remote sensing instruments on the **H**igh **A**ltitude **L**ong Range Research Aircraft (HALO).

In this work, the measurements of the passive radiometer component of **H**ALO **M**icrowave **P**ackage (HAMP) were used to derive IWV and individual cloud LWP. The statistical retrieval performance was evaluated by comparison to coincident dropsonde measurements in case of IWV, and by performance analysis in clear-sky conditions in case of LWP, respectively. The analysis showed that HAMP is suitable to resolve the variability of tradewind cumuli. Exploiting the synergy of remote sensing instruments on HALO, a cloud mask algorithm was developed based on radiance measurements by **H**ALO-**S**olar **R**adiation (HALO-SR), and cloud statistics were derived, matching the observations of other authors.

Coincident spaceborne observations by the **S**pecial **S**ensor **M**icrowave **I**mager/**S**ounder (SSMIS) and the **M**ODerate **I**maging **S**pectroradiometer (MODIS) were evaluated. This study revealed that SSMIS's coarse resolution is sufficient to cover IWV characteristics, but not small-scale LWP variability. MODIS LWP, derived with a finer resolution, covered the LWP spatial variations but suffered from known discrepancies between optical and microwave retrievals.

Contents

1	Introduction	3
2	Basics	7
2.1	Maritime Cumulus Clouds in the Tradewinds	7
2.2	Atmospheric Radiation	10
2.3	Cloud Remote Sensing Applications	14
3	NARVAL campaign	19
3.1	Overview	19
3.2	HALO Microwave Package (HAMP)	21
4	Airborne derived cloud properties	25
4.1	Vertically integrated properties	25
4.1.1	HAMP Retrieval Development and Sensitivities	25
4.1.2	IWV Retrieval Evaluation	30
4.1.3	LWP performance analysis	35
4.2	Cloud Properties Exploiting Sensor Synergy	40
4.2.1	Synergy potential	40
4.2.2	Horizontal Cloud Properties	44
5	Satellite Product Evaluation	49
5.1	SSMIS IWV and LWP products	49
5.1.1	Data Description	49
5.1.2	Direct Overpass Analysis	50
5.1.3	Regional Distributions	55
5.2	MODIS LWP	58
5.2.1	Data Description	58
5.2.2	Performance Example	59
5.2.3	Direct Overpasses Analysis	63
6	Conclusion and Outlook	67
A	HAMP Technical Specifications	71
	Bibliography	73

List of Abbreviations

Abbreviation	Description
AMSR-E	Advanced Microwave Scanning Radiometer-Earth Observing System.
ASTER	Spaceborne Thermal Emission and Reflection Radiometer.
DIAL	Differential Absorption Lidars.
DMSF	Defense Meteorological Satellite Program.
ECMWF	European Centre for Medium-Range Weather Forecasts.
GCM	Global Climate Model.
HALO	High Altitude and Long Range.
HALO-SR	HALO - Solar Radiation.
IPCC	Intergovernmental Panel on Climate Change.
ITCZ	Innertropical Convergence Zone.
IWV	Integrated Water Vapor.
JOYCE	Jülich Observatory for Cloud Evolution.
LES	Large Eddy Simulation.
LIDAR	Light Detection And Ranging.
LWP	Liquid Water Path.
MODIS	Moderate Imaging Spectroradiometer.
NARVAL	Next Generation Aircraft Remote-sensing for VALidation studies.

Abbreviation	Description
NASA	North American Space Agency.
NeDT	Noise equivalent Delta Temperature.
PAMTRA	Passive and Active Microwave Transfer model.
RADAR	Radio Detection And Ranging.
RICO	Rain In (shallow) Cumulus over the Ocean.
RMS	Root Mean Square error.
RSS	Remote Sensing Systems.
RTE	Radiative Transfer Equation.
SSMIS	Special Sensor Microwave Imager/Sounder.
SST	Sea Surface Temperature.
TRMM	Tropical Rainfall Measuring Mission.

List of Figures

1.1	Typical shallow cumulus clouds	5
2.1	Circulation Pattern and temperature	8
2.2	Scattering size parameter	12
3.1	NARVAL South Research Flights	19
3.2	HALO and NARVAL instrumentation	20
3.3	Simulated brightness temperature spectrum with HAMP frequencies	22
3.4	HAMP footprint size	23
3.5	HAMP measurements during RF06, 16.12.2013	24
4.1	LWP and IWV retrieval strategy	26
4.2	IWV and LWP theoretical retrieval error	28
4.3	Retrieval Sensitivity to SST	29
4.4	Retrieval Sensitivity to TB error	30
4.5	Estimation of missed IWV due to flight altitude	31
4.6	Performance example for HAMP and dropsonde IWV measurements	32
4.7	Uncertainty estimation of HAMP IWV with K7 and 90	33
4.8	Uncertainty of HAMP IWV in different channel combinations	34
4.9	Theoretical RMS for LWP	35
4.10	Clear-sky HAMP LWP distribution	36
4.11	HAMP retrieved LWP distribution in clear and cloudy scenes	37
4.12	Example Performance of HAMP and HALO-SR	39
4.13	Example Performance of HAMP and HALO-SR	41
4.14	Example Performance of HAMP and HALO-SR in case of evaporating precipitation	42
4.15	HALO-SR increased sensitivity to cloud edges	43
4.16	Cloud Mask Performance Example	44
4.17	Difference in cloud length occurrence for two regions	45
4.18	Cloud Length Distribution	45
4.19	Double logarithmic Cloud Size Distribution	47
4.20	Cloud LWP Distribution	47

List of Figures

4.21	Combined Cloud Length-LWP Distribution	48
5.1	Map of Descending SSMIS Swath, 15.12.2013	51
5.2	Case study of SSMIS and HAMP coincident measurements	52
5.3	Direct Overpass Comparison HAMP and SSMIS	53
5.4	HAMP and SSMIS descending orbit distributions	56
5.5	Aqua MODIS swath, 11.12.2013, 17:20 UTC	59
5.6	Case study comparison of HAMP and MODIS LWP, RF02	60
5.7	Case study comparison of HAMP and MODIS LWP, RF06	61
5.8	HAMP passive and active measurements, RF06	62
5.9	HAMP MODIS LWP comparison	63

List of Tables

2.1	Literature Results for power law exponent λ	10
5.1	Details for comparison between all coincident measurements by HAMP and SSMIS with less than one hour of time difference between the measurements.	54
5.2	Details for comparison between all coincident measurements by HAMP and Aqua MODIS with less than 10 and 5 minutes time difference, respectively.	64
A.1	HAMP characteristics	71

1 Introduction

Clouds appear all over the globe in various shapes, sizes, and characteristics. Ranging from popcorn and sheep clouds to horizontally extended stratus clouds and thunderstorm cumulonimbi, they cover two thirds of the globe (Rossow and Schiffer [1999]). Clouds not only influence our daily lives, as when we decide whether to take an umbrella or a sunhat, but also impact the world on a large scale, modulating radiation, weather, the hydrological cycle - the climate (Jiang et al. [2012], Hartmann et al. [1992]).

The state of global climate change, surveyed by the **I**ntergovernmental **P**anel on **C**limate **C**hange (IPCC), is reviewed in the IPCC-report, most recently in 2013 (Stocker et al. [2013], Boucher et al. [2013]). Therein, clouds and aerosols "continue to contribute the largest uncertainty to estimates and interpretations of the Earth's changing energy budget" modeled by **G**lobal **C**limate **M**odels (GCM) (Boucher et al. [2013], p 573).

The effects of global climate change on the hydrological cycle and its drivers are not yet well captured in climate sensitivity studies. Large intermodel spreads occur, partly due to lapse rate feedbacks driven by water vapor (Soden and Held [2006]) and precipitation amount (Wentz et al. [2007]), but to a larger extent of up to 70 % by cloud feedback uncertainties (Vial et al. [2013], Bony et al. [2015], Zhang et al. [2005]). Primarily, the response to climate change of warm shallow clouds prevailing in the subtropical tradewind driven region to changing environmental conditions constitutes a major source of uncertainty in these studies (Bony and Dufresne [2005], Bony et al. [2015]). These clouds, widely known as tradewind clouds, prevail in the tradewind-regions between the equator and 30 °N and 30 °S, respectively.

Shallow cumulus processes can be resolved in **L**arge **E**ddy **S**imulations (LES) (Neggers et al. [2003a]). Due to coarser spatial resolution of GCMs, these processes are included via parametrisation (Arakawa [2004], Sato et al. [2015], Tompkins [2002]). As widely observed, e.g. by Chepfer et al. [2008] and Naud et al. [2010], GCM models, however, do not fully represent satellite observations of e.g. cloudiness and, thus, require improvement in parametrisation. This can only be achieved

by more detailed observations of cloud properties and the cloud size distribution (Neggers et al. [2003b]).

Tradewind marine boundary layer clouds are low in total cloud liquid (**L**iquid **W**ater **P**ath, LWP) with hardly more than 1000 gm^{-2} (Rauber et al. [2007]). It is not yet fully understood if and how much precipitation they produce (Nuijens et al. [2009]). Turner et al. [2007] and Sengupta et al. [2003] state that especially LWP variations in low LWP clouds, however, influence radiative fluxes to a high degree, and, thus, need to be observed with high precision.

Whereas in-situ measurements of clouds are limited to small scale analysis, remote sensing applications offer wide possibilities to characterise clouds and precipitation on a larger spatial scale (Stubenrauch et al. [2013]). Over the oceans, the potential for groundbased observations is limited to buoys or shipbased measurements (e.g. Zuidema et al. [2005]), which are often expensive and have limited temporal coverage (Lammert and Ament [2015]). To overcome these limitations, synergies of passive and active instruments are gaining importance for surface-based platforms (Löhnert et al. [2014]) and air- and spaceborne observations (Parkinson [2003]), allowing to monitor cloud structure and integrated quantities simultaneously.

Observations by Earth-observing satellites, covering a vast spatial and temporal scale, have successfully contributed to a more profound analysis of clouds and precipitation (Lin and Rossow [1994]). Yet, it is still challenging to quantify uncertainties of the derived geophysical parameteres due to retrieval differences and constraints such as model assumptions and cloud mask performance difficulties (Stephens and Kummerow [2007]). Investigating the impact of spatial resolution on cloud fraction observations, Wielicki and Parker [1992] found that large discrepancies, especially for shallow boundary layer clouds, occur for pixel sizes larger than 1 km^2 .

LWP can be retrieved from solar reflectances or microwave emissions, but differences in the observations of warm maritime clouds occur as analysed by Horváth and Gentemann [2007], Seethala and Horváth [2010] and Borg and Bennartz [2007]. The authors state that uncertainties in the microwave retrieval developed by Wentz [1997] are partly caused by cloud absorption and cloud-rain partitioning assumptions (O'Dell et al. [2008]) and background emissivity dependencies. Errors in the optical retrieval based on the Nakajima and King [1990] approach can e.g. occur due to 3D scattering effects at low solar zenith angles and the assumption of vertical cloud homogeneity (Bennartz [2007]).

Therefore, the arising question is how satellite retrieval products of LWP and Integrated Water Vapor amount (IWV) can be independently evaluated to increase the accuracy in the observations for retrieval and model verification (Greenwald [2009], Stephens and Kummerow [2007]).

According to Mech et al. [2014] and Lammert and Ament [2015], airborne derived cloud properties using a combination of active and passive sensors offer great potential for satellite data evaluation due to fine resolution and highly flexible measurements. Mech et al. [2014] introduce the **HALO Microwave Package (HAMP)** instrument, which combines a cloud radar with a microwave radiometer capturing emission in 26 channels up to 200 GHz. HAMP and other remote sensing instruments were installed on the **High Altitude Long Range Research Aircraft (HALO)**. During the analysed **Next Generation Aircraft Remote-sensing for VALidation studies (NARVAL)-South** campaign in December 2013, shallow tradewind cumuli were observed (Klepp et al. [2014]). Figure 1.1 shows an example of these clouds observed during the campaign. The collected data offers potential to evaluate coincident satellite measurements and exploit sensor synergy to both characterize individual clouds, and derive cloud statistics in the overflowed regions.



Figure 1.1 – Typical shallow cumuli observed in the tradewinds (Klepp et al. [2014]).

The purpose of this work is to answer the following questions:

- How can airborne observations performed with HAMP’s passive radiometer during the NARVAL-South campaign be exploited to derive water vapor characteristics and individual cloud properties, resolving the high variability of shallow tradewind cumuli?
- How can the synergy of active and passive remote sensing devices on HALO improve the derivation of horizontal and vertical cloud properties, and statistics?
- Do coincident spaceborne observations by the **Special Sensor Microwave Imager/Sounder (SSMIS)** with a coarser resolution and the **MODerate Imaging Spectroradiometer (MODIS)** with a similar resolution to HAMP, respectively, represent the airborne derived properties accurately?

Therefore, the thesis is structured in the following way. First, an overview of the expected tradewind cloud properties, atmospheric radiation, and remote sensing applications will be given in chapter 2. The NARVAL campaign goals and instrumentation will be described in chapter 3. Vertical and horizontal cloud properties derived from HAMP data in synergy with other sensors during NARVAL-South will be analysed in chapter 4. A comparison to spaceborne applications will be given in chapter 5. The results of the thesis will be summarised and potential for future work will be presented in chapter 6.

2 Basics

This chapter gives an overview about tradewind clouds, atmospheric radiation and the potential to observe clouds using remote sensing strategies. First, the formation of maritime boundary layer clouds in the subtropics and their properties will be presented in section 2.1. The principles of atmospheric radiation will be presented in section 2.2, introducing the concept of radiative transfer. Applications to observe clouds and their properties exploiting remote sensing strategies will be reviewed in section 2.3.

2.1 Maritime Cumulus Clouds in the Tradewinds

Blowing steadily between the equator and up to 30°N and 30°S , respectively, the tradewinds transport maritime moist air poleward, forming a part of the Hadley circulation which determines the large-scale dynamic processes in the tropics and subtropics (Roedel [2000], p 129).

Strong solar income close to the equator triggers deep convection of moist and warm air, leading to a high precipitation amount. Ascending air close to the equator leads to surface flows towards the equator due to mass continuity. This zone, forming the ascending branch of the Hadley circulation, is called the **Inner Tropical Convergence Zone (ITCZ)**, seasonally migrating north- and southwards around the equator with a maximum extension during the respective hemisphere's summer (Stevens et al. [2015]).

Closing the cycle of the Hadley pattern, relatively dry air from convection and precipitation flows poleward in high altitudes, cools, and descends, warming dry-adiabatically, in the subtropical latitudes ranging up to 30°N and 30°S , respectively. This dry descending air leads to the formation of a subtropical capping inversion layer at 2-3 km, increasing in height when approaching the equator. Separating moist and dry air, this layer limits the vertical expansion of the boundary layer, suppressing convection processes and cloud formation above the inversion base height. Close to the western continental coastlines, stratocumulus clouds prevail, breaking up into cumulus clouds over the oceans, known as tradewind cumuli (see fig. 2.1). These

clouds can be well observed around Barbados and the Atlantic ocean, being exposed to the easterly tradewinds conditions especially in the northern hemisphere winter (Stevens et al. [2015]).

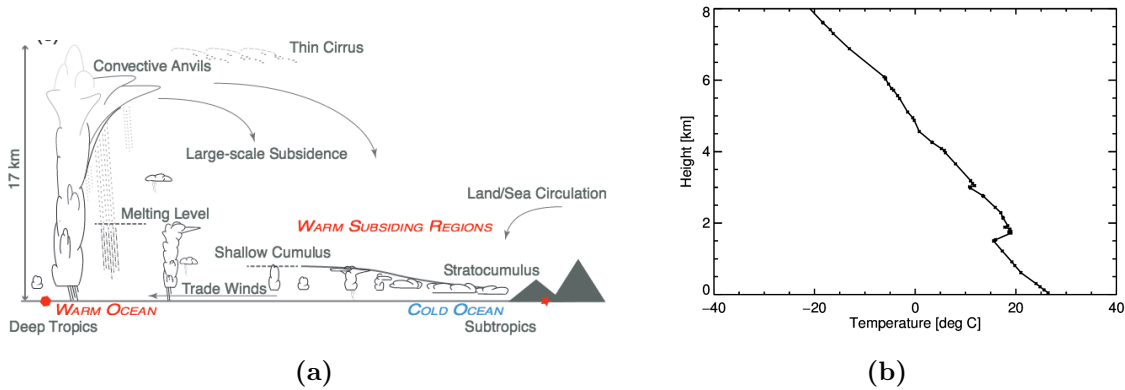


Figure 2.1 – (a) Typical circulation pattern driven by the Hadley cell in tropical and subtropical latitudes, determining cloud formation (Boucher et al. [2013], p 579). Warm subsiding air leads to the typical subtropical (b) temperature inversion layer around 1.5 km altitude. The profile was measured over Barbados, Grantley Adams Airport (13.08 °N, -59.49 °W), observed by an ascending radiosonde 10.12.2013, 12 UTC.

Even though tradewind clouds are temporally and spatially limited in size and range (Stevens [2005]), they are not only of particular interest for regional weather processes, but also for the subtropical climate. Driving vertical mixing processes in the boundary layer, they provide part of the moisture transported to the center of the ITCZ by the tradewinds, and are an important part of the hydrological cycle in this region (Betts [1997]).

As the air below the inversion layer typically does not reach a temperature below freezing level (see fig. 2.1b), shallow clouds do not contain ice particles. In the absence of high-reaching convection and high clouds, the atmosphere, thus, is hydrologically mainly composed of water vapor and liquid water. The total amount of water vapor in a vertical column through the atmosphere above a unit surface area is called **I**ntegrated **W**ater **V**apor (IWV). The **L**iquid **W**ater **P**ath (LWP) describes the total amount of liquid water within a normalised atmospheric column, which can either originate from cloud droplets, drizzle, or precipitation.

Trenberth et al. [2005] found a yearly mean IWV of $30 - 40 \text{ kgm}^{-2}$ in the easterly tradewinds east of Barbados. They analysed the SSMIS climatology of global water vapor distribution and compared it to **E**uropean **C**entre for **M**edium-**R**ange **W**ather **F**orecasts (ECMWF) **R**e-**A**nalysis (ERA) data. An overestimation of ERA compared to SSMIS of up to 1 kgm^{-2} was observed. Due to the seasonal cycle of the ITCZ,

leading to humid summers and dry winters on the northern hemisphere, it can be expected that the observed IWV during the NARVAL campaign lies below this year average value.

Current knowledge about tradewind cloud properties is almost entirely based on satellite-derived measurements, as field studies are rare (Stevens et al. [2015]). Observations during the **R**ain **I**n (shallow) **C**umulus over the **O**cean campaign (RICO, Rauber et al. [2007]) revealed that LWP of these clouds hardly ever reaches 1000 g/m^2 with mean sized droplets ranging from $1 - 5 \mu\text{m}$ (Arabas et al. [2009]). According to Turner et al. [2007], low-level clouds without ice often contain an LWP of less than 100 g/m^2 .

Shallow clouds are assumed to be mostly precipitation free (Betts [1997]). However, based on two months of groundbased radar observations, Nuijens et al. [2009] estimate that more than half of the total observed precipitation originated from shallow clouds. Rauber et al. [2007] found that precipitation from shallow cumuli might often be missed by active remote sensing satellite measurements such as the **T**ropical **R**ainfall **M**easuring **M**ission (TRMM) radar.

According to Wood and Field [2011], the tradewind driven regions of the world contain the smallest clouds, with 50 % of the clouds having lengths of 10 km and below. Analysing 15 m-resolved infrared data delivered by the **A**dvanced **S**paceborne **T**hermal **E**mission and **R**eflection **R**adiometer (ASTER), Zhao and Di Girolamo [2007] even found that 50 % of the observed clouds had an equivalent area diameter of less than 2 km.

The occurrence probability $p(l)$ of a cloud with length l can be described by a power law (equation (2.1.1)).

$$p(l) = al^{-\lambda} \tag{2.1.1}$$

This relation was confirmed by recent studies by the authors listed in table 2.1. The authors also found scale breaks in the size distributions of clouds, separating the distribution of small and large clouds which are, however, not constant between the different measurements. Other relation, such as an exponential law found by Wielicki and Welch [1986], have not been confirmed by recent observations.

Table 2.1 – Observed results for the power law exponent λ depending on the data resolution.

reference	method	λ
Zhao and Di Girolamo [2007]	spaceborne	2.19
Benner and Curry [1998]	air- and spaceborne	1.98
Wood and Field [2011]	air- and spaceborne	1.66
Neggens et al. [2003b]	LES	1.70

The exponent λ depends on the resolution and binning of the data (Zhao and Di Girolamo [2007]) and is obtained by fitting equation (2.1.1) to the observed distribution, usually represented in a double logarithmic representation. So far, exponents with $\lambda \approx 2$ have been reported by differently resolved measurements exploiting satellite and airborne observations as well as LES modeling (see tab. 2.1).

2.2 Atmospheric Radiation

Radiation around us on Earth is ubiquitous (Petty [2006], p 6), and is of "fundamental importance to the global climate" (Petty [2006], p 49). The Earth's radiation budget is controlled by the balance between solar shortwave emission and thermal longwave radiation emitted by the Earth and atmosphere (Petty [2006], pp 6, pp 132). Shortwave radiation in the visible and near-infrared spectrum is characterised by wavelengths smaller than $4 \mu\text{m}$, whereas longwave microwave rays have wavelengths of larger than 1 mm and frequencies larger than 3 GHz, respectively (Petty [2006], p 58).

Every object with a temperature T emits radiation at multiple frequencies which is described by Planck's law (Petty [2006], pp 114). Perfectly emitting bodies, so-called blackbodies, emit the maximum possible radiation with intensity B , which depends on the frequency ν and the temperature T of the emitting body (see eq. 2.2.1 with h : Planck constant, k : Boltzman constant, c : speed of light).

$$B(\nu, T) = \frac{2h\nu^3}{c^3} \frac{1}{e^{\frac{h\nu}{kT}} - 1} \quad (2.2.1)$$

However, not all bodies are perfect emitters, but their emitted radiation I will deviate from the predicted Planck radiation B by a factor ϵ , the emissivity which is

body-characteristic and frequency-dependent (equation (2.2.2), Petty [2006], p 123). Typical assumed surface emissivity values for microwave emissivities are $\epsilon \approx 0.95$ for dry land, and $\epsilon \approx 0.50$ for ocean (Janssen [1993], p 286). The ocean emissivity depends on the roughness of the surface, influenced by the **Sea Surface Temperature** (SST) and wind speed v_w .

$$I(\nu, \text{SST}, v_w, T) = \epsilon(\nu, \text{SST}, v_w)B(\nu, T) \quad (2.2.2)$$

In the spectral microwave region, the shape of the Planck function can be linearly approximated by the Rayleigh-Jeans approximation if the condition $h\nu \ll kT$ is fulfilled (equation (2.2.3), adapted from Demtröder [2000], p 77).

$$B_{RJ}(\nu, T) = \frac{2\nu^2}{c^3}kT \quad (2.2.3)$$

Inserting this relation into equation (2.2.2), the brightness temperature can be defined as the emitter's radiation-equivalent temperature. Therefore, the brightness temperature T_B of a body at a frequency ν will linearly depend on the physical temperature of the emitter (equation (2.2.4), Petty [2006], p 152).

$$T_B(\nu) = \epsilon(\nu)T \quad (2.2.4)$$

When propagating through the atmosphere, a ray of incident light will interact with the atmospheric components via scattering and absorption processes, characterised by the frequency dependent coefficients β_s and β_a , respectively (Petty [2006], pp 155). The total attenuation is, then, described by the extinction coefficient $\beta_e = \beta_a + \beta_s$. Along an infinitely small path ds through an atmospheric layer, the change of intensity due to extinction is described by equation (2.2.5).

$$\frac{dI_{ext,\nu}}{ds} = -\beta_{e,\nu}(s)I_\nu(s) \quad (2.2.5)$$

Integrating this equation and introducing the opacity τ as the total extinction between s_1 and s_2 (equation (2.2.6)) leads to Beer's law (equation (2.2.7)), describing the attenuated intensity by extinction.

$$\tau_\nu(s_1, s_2) = \int_{s_1}^{s_2} \beta_{e,\nu}(s) ds \quad (2.2.6)$$

$$I_\nu(s_1, s_2) = I_\nu(s_1) e^{-\tau_\nu(s_1, s_2)} \quad (2.2.7)$$

Scattering processes occur because atmospheric particles interact with electromagnetic radiation, and depend on the scatterers' radius r , their shape, dielectric properties, and the wavelength λ of the incident ray (Petty [2006], pp 345). The size parameter $x = \frac{2\pi r}{\lambda}$ combines these parameters, giving information about the significance of scattering processes (figure 2.2). Whereas particles like dust and cloud droplets are strong scatterers in the visible and infrared regimes, leading e.g. to the blue color of the sky, they negligibly scatter in the microwave spectral range (Janssen [1993], p12). The extinction coefficient β_e , thus, simplifies to $\beta_e \approx \beta_a$.

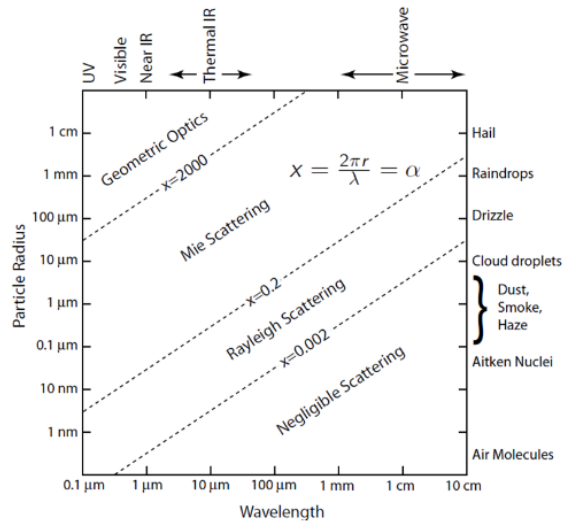


Figure 2.2 – Dependency of scattering properties on radiation frequency, wavelength and particle size (Petty [2006], p 346).

Absorption of radiation occurs at frequencies which excite vibrational or rotational molecular energy state transitions with a needed energy of $\Delta E = h\nu$ (Petty [2006], p 240). The main absorbers in the microwave range are oxygen and water vapor, exciting rotational transitions at 60 and 118.75 GHz, and 22.23 and 183.3 GHz, respectively. Under atmospheric pressure, molecules collide with other molecules, leading to the so-called pressure broadening of the discrete absorption lines to absorption complexes (Petty [2006], p 263). Additionally, continuum absorption by water in both its liquid and gaseous states increases with the frequency squared in the microwave spectral range (Janssen [1993], p 70).

Following Kirchhoff's law, absorbing bodies in local thermodynamic equilibrium emit radiation to the same amount as they absorb it (Petty [2006], p 125). The emissivity ϵ , thus, equals the absorptivity of the body, which depends on its mass (Petty [2006], pp 165) and the radiation's frequency. Therefore, atmospheric gases emit radiation following Planck's law with the intensity B_e , depending on the gas's temperature and pressure, and absorption frequency (Petty [2006], pp 114). The emitted radiation along the path ds is formulated by equation (2.2.8).

$$\frac{dI_{emit,\nu}}{ds} = \beta_a B_e(\nu, T) \quad (2.2.8)$$

The net change of propagating radiation with intensity I through the atmosphere along a path ds , thus, comprises extinction and emission effects, here neglecting scattering effects. Considering equation (2.2.5) for the absorption part and equation (2.2.8) for the emission-induced change, the total net change is summarised by the Schwarzschild equation (equation (2.2.9), Petty [2006], pp 205)

$$\frac{dI_\nu}{ds} = \frac{dI_{emit}}{ds} + \frac{dI_{ext}}{ds} = \beta_a(B_{\nu,e} - I_\nu) \quad (2.2.9)$$

Integrating the Schwarzschild equation through an entire atmospheric column, more generally the **R**adiative **T**ransfer **E**quation (RTE) is used to describe the contributions to intensity change. Assuming a plane-parallel atmosphere¹, neglecting scattering processes, the RTE for a nadir-looking satellite at z_{sat} with zenith observation angle is formulated by equation (2.2.10) (Janssen [1993], pp 273), describing the observed brightness temperature $T_{B,sat}$ at the satellite's position.

$$T_{B,sat}(\nu) = T_{B,ground}(\nu)e^{-\tau_\nu(z_0,z_{sat})} + \int_{z_0}^{z_{sat}} \beta_a(\nu, z)e^{-\tau_\nu(z,z_{sat})}T(z)dz \quad (2.2.10)$$

The measured brightness temperature depends on two main components: the background emission $T_{B,ground}$ of the underlying surface attenuated by the total atmosphere's opacity, and the atmospheric emissions depending on the temperature

¹This approximation is assumed to be valid as the atmospheric temperature T is sufficiently horizontally stratified.

T of the emitter, attenuated by the total opacity of the atmospheric column between the emitter and the sensor's position.

2.3 Cloud Remote Sensing Applications

Remote sensing applications gather information about a target without getting into physical contact with it (Chuvieco and Huete [2009], p 21), exploiting electromagnetic radiation. Measurements are performed surfacebased on the ground (e.g. Löhnert et al. [2014], Ackerman and Stokes [2003]) or ship (e.g. Zuidema et al. [2005]), and from the air (e.g. Mech et al. [2014]) and space (e.g. Stephens et al. [2002], Hollinger et al. [1990]). Compared to in-situ measurements they offer a variety of advantages by providing large spatial or temporal resolution, and cover remote areas of the globe (Stubenrauch et al. [2013]).

Commonly, instruments are discriminated as active or passive devices. Whereas active instruments send out radiation at a specific frequency and collect the reflected beams, passive sensors receive the naturally occurring radiation at a specific frequency (Chuvieco and Huete [2009], p 63). Depending on the frequencies used, a wide variety of atmospheric and Earth-properties can be retrieved, such as e.g. vegetation cover, ocean characteristics, but also cloud cover, atmospheric gas concentrations and temperature and humidity in different atmospheric layers (e.g. Petty [2006] p 8, Stephens [1994], p3).

Cloud remote sensing is performed with active and passive sensors, combining different instruments' advantages. Depending on the frequency they operate at, active sensors can deliver the hydrometeor structure within an atmospheric column, whereas passive sensors are more frequently used to capture integrated parameters (Cimini et al. [2010], pp 25; pp 35).

Prominent examples for active cloud remote sensing devices are the **L**Ight **D**etection **A**nd **R**anging (Lidar) and the **R**ADio **D**etection **A**nd **R**anging (Radar). While the former emits and receives radiation in the visible and near-infrared spectral range, the latter senses radiation in the microwave range. Both instruments are based on the same principle of emitting pulses of radiation at a certain frequency and receiving backscattered signal. From this backscattered signal, microphysical properties and cloud boundaries can be derived.

Lidars can have different configurations, depending on the parameter under study. **Differential Absorption Lidars (DIAL)** operate at two wavelengths, one close to the absorption complex center, one located further on the wing. By calculating the differential absorption coefficient, the concentration of the corresponding absorber gas in the vertical column can be estimated. For example, this technique is successfully applied to derive water vapor concentrations (Wirth et al. [2009]) or ozone distributions (Browell et al. [1998]).

In the microwave range where the radar operates in, the power of the backscattered signal P_b depends on the reflectivity factor Z . This factor is determined by the diameter D of the scatterer to the power of six and the concentration of scatterers along the beam path $n(D)$, assuming spherical particles and Rayleigh scattering (equation (2.3.1), Petty [2006], pp 379). The distance to the hydrometeor can be calculated from the time difference between emitting and receiving each pulse. Thus, a change in hydrometeor size e.g. due to drizzle or precipitation events highly influences the reflectivity, and thus, the backscattered power, scaled with the power of six.

$$P_b \propto Z = \int_0^{\infty} n(D)D^6 dD \quad (2.3.1)$$

Radar and lidar are sensitive to different particle sizes because of their different emitted frequencies. The smaller the wavelength of the emitted beam, the smaller the particles are which can be detected by the instrument (Battan [1973], p 3), leading to a higher sensitivity to cloud droplets by the lidar than by the radar.

However, water molecules are very opaque in the visible and near-infrared spectral range, which is why lidar emitted beams cannot penetrate thick clouds. This opacity limits the vertical range of the instrument in cloudy conditions. Nonetheless, this feature can be used to detect the cloud base or top height with high accuracy using surface- or air-/spaceborne ceilometers, respectively.

Radars, in contrast, penetrate clouds and, basing on equation (2.3.1) and the operating frequency, derive the hydrometeor structure within the entire vertical column. Two common atmospheric applications exist: precipitation radars operating at a frequency of 10 GHz, resolving rain droplets with negligible impact by cloud droplets, and cloud radars operating at 35 or 90 GHz, which can sense cloud droplets (Cimini et al. [2010], p33, Melchionna et al. [2008]). However, investigations show

that they can miss small clouds as the reflectivity of the low amount of small cloud droplets does not lead to a backscattered signal above the detection limit (Clothiaux et al. [2000]). Doppler radars can also measure the vertical falling velocity of a scattering hydrometeor by resolving the Doppler shift in the received frequency compared to the emitted one (Battan [1973], p114).

In contrast to active sensors, passive remote sensing applications such as spectrometers or radiometers, detect naturally emitted radiation in different frequency ranges. Nadir-looking sensors which are sensitive to radiation in the visible and near-infrared spectrum, sense reflected sunlight from clouds or the ground, whereas microwave devices detect radiation emitted by atmospheric constituents or the surface. Referring to the RTE (equation (2.2.10)), background emission will contribute to the observed signal.

Examples for passive instruments operating in the visible and near-infrared are the spaceborne **MOD**erate resolution **Im**aging **S**pectroradiometer (MODIS) or the airborne **HALO** Solar **R**adiation (HALO-SR) instrument. In clear scenes, characteristics of the ground can be determined, such as vegetation properties over land (e.g. Huete et al. [2002]) and ocean features (e.g. Esaias et al. [1998]). In cloudy scenes, however, the atmosphere is highly opaque, so that mainly reflected radiation by clouds reaches the sensor. Combining information from an absorbing and a non-absorbing frequency, the retrieval of cloud droplet effective radius r_{eff} and optical depth τ , respectively, is possible following the strategy developed by Nakajima and King [1990].

Following equation (2.3.2) (Nakajima et al. [1991]) with ρ_{liquid} as density of liquid water, Liquid Water Path (LWP) is defined as the total amount of liquid water in a vertical column above a unit surface. It linearly depends on the retrieved parameters τ and r_{eff} assuming a vertical homogeneous cloud and a cloud droplet extinction efficiency of $Q_e \approx 2$.

$$LWP = \frac{2}{3} \rho_{\text{liquid}} r_{\text{eff}} \tau \quad (2.3.2)$$

Due to the opacity of the clouds, the penetration depth of radiation at a water absorbing wavelength decreases the stronger the absorption is (Platnick [2000]). Assuming vertical homogeneity, the derived effective radius from cloud top is valid for the entire column. As pointed out by Bennartz [2007], however, this approach

introduces uncertainties for vertically inhomogeneous clouds, as the effective radius of the cloud droplets varies with cloud depth depending on the droplet distribution. In case of increasing r_{eff} with cloud depth, the retrieved LWP underestimates the actual amount of water.

Passive remote sensing based on microwave emissions offers advantages, because radiation can penetrate clouds and delivers measurements even if the sun is not present (Ulaby et al. [1981], p 1). Thus, atmospheric parameters such as temperature and humidity can be derived in any weather circumstances (Cimini et al. [2010], p 18). These parameters are obtained when inverting the RTE (equation (2.2.10)), matching a specific atmospheric state to an observed set of brightness temperatures. As this problem is underdetermined and not explicitly solvable, retrieval algorithms are often built basing on statistical a-priori knowledge (Stephens [1994], pp 6 ; Cimini et al. [2010], pp 23).

Following the Rayleigh-Jeans approximation (equation (2.2.3)), the observed brightness temperature at absorption frequencies depends on the temperature of the emitter. Absorption complexes such as oxygen around 60 GHz can, thus, be used to retrieve temperature profiles. Similarly, information from water vapor absorption is used to retrieve humidity using the pressure-broadened 22.2 GHz line. Integrated quantities like IWV and LWP can be derived using channels which are sensitive to the entire column (Cimini et al. [2010], p 25). The retrieval of LWP is based on the fact that the continuum absorption of water increases with the frequency squared, so that the combination of a window and a water vapor absorption channel will give information about the contributions from water vapor and liquid water, respectively (Westwater [1978]).

In all passive microwave applications, background emissivity needs to be considered as an additional signal source (see eq. 2.2.10). For surface-based devices, the background can be approximated by the cosmic background. In air- and spaceborne applications, however, the background emissivity depends on the particular overpassed scene, and is generally higher over land than over ocean (Janssen [1993], p 286). Over the radiatively dark ocean, clouds lead to an increase in the observed brightness temperature with a higher gradient than in a similar case over land.

As the wide variety of atmospheric processes occur on scales ranging from a few milliseconds to days and millimeters to thousands of kilometers, the different measurement requirements can best be combined by synergising different observation methods, exploiting their different strengths to gain an optimal understanding of

these processes (e.g. Cimini et al. [2010], pp 129). Therefore, satellite platforms such as the **N**orthern **A**merican **S**pace **A**gency's (NASA) Aqua (Parkinson [2003]), cloud observatories such as the **J**ülich **O**bservator**Y** for **C**loud **E**volution (JOYCE; Löhnert et al. [2014]) or airborne platforms like the **H**igh **A**ltitude and **L**Ong Range (HALO) aircraft synergise active and passive instruments in order to capture atmospheric processes as accurately as possible.

3 NARVAL campaign

In the following chapter, the Next Generation Aircraft Remote-sensing for VALidation studies (NARVAL) campaign will be introduced, performed with the german research aircraft HALO. First, an overview about the campaign, its goals and the used instrumentation will be given in section 3.1. The HALO Microwave Package (HAMP) will be described in detail in section 3.2 giving information about the instrument's properties, advantages and potential.

3.1 Overview

The NARVAL mission's main scientific goal, following Klepp et al. [2014], is to gain a "better understanding [of] the prevalence and structure of clouds and precipitation from shallow convection in two large-scale regimes". Therefore, HALO (see fig. 3.2) was equipped with remote sensing instruments and performed 15 research flights during two separate campaigns. Eight flights took place in the atlantic tradewind region east of Barbados in December 2013

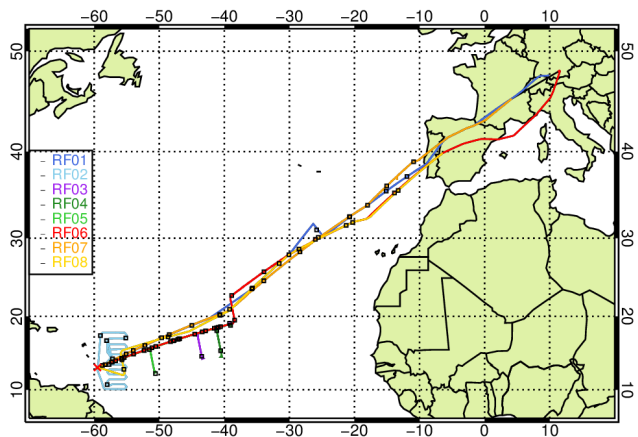


Figure 3.1 – Dropsonde releases (black) and HALO flight routes of the eight research flights performed during NARVAL South from 10.12. - 21.12.2013.

for NARVAL-South, the other seven were performed during NARVAL-North over convective weather regions around Iceland in January 2014.

The tracks of the NARVAL-South research flights are shown in figure 3.1 and included regional flights east of Barbados as well as transatlantic flights between Grantley Adams Airport, Barbados and Oberpfaffenhofen, Germany. Specific legs were included in the flight routes to observe scenes of overpassing satellites from e.g.

the A-Train constellation, including the satellite Aqua with the instruments MODIS and AMSR-E.

The goal of NARVAL-South was not only to observe shallow, non-precipitating cumulus clouds in the north-eastern tradewinds during the dry season, but also to evaluate the possibilities of using HALO as an airborne remote sensing platform by combining airborne observations to coincident, independent measurements. Using overpassing satellite data, the campaign results have the potential to help limit uncertainties of cloud representation in forecast and climate models by evaluating broader resolution satellite products with HALO based measurements (Klepp et al. [2014]).



Figure 3.2 – (a) HALO with NARVAL-South instrumentation (DLR [2006b]). (b) Bellypod instrumentation, from left to right: HAMP-G, HALO-KV, HALO-WF modules, WALES lidar and MIRA cloud radar (Mech et al. [2014])

As a research platform, HALO offers multiple advantages due to its long range and high carrying weight potential. During the campaign, the aircraft flew at altitudes between 10 to 14 km with an average ground speed of 220 m/s. Due to close mounting of the different sensors with their different advantages as pointed out in section 2.3, the data offers high analysis potential, also by exploiting sensor synergy.

HAMP consists of three nadir-looking passive radiometers and an active component, a 36 GHz cloud radar (Mech et al. [2014]), combining passive, column-integrating measurements with an active, vertically resolving component. Additionally, a multi-wavelength water vapor differential absorption lidar (WALES, Wirth et al. [2009]) was installed next to HAMP in a bellypod under HALO (figure 3.2). Radiance measurements in the solar and near-infrared range were performed in six channels by **HALO-Solar Radiation** (HALO-SR) through two optical inlets installed on top and at the bottom of the aircraft (Fricke et al. [2014]). **Differential Optical Absorbption**

Spectroscopy was performed by a mini-DOAS, measuring the 2D-distribution of trace gases (Weidner et al. [2004]). The momentary atmospheric state was recorded by the **BA**sic **HALO** **M**easurement **A**nd **S**ensor System BAHAMAS, recording temperature and humidity close to the aircraft (DLR [2006a]). Vertical temperature and humidity profiles of chosen scenes were obtained with 75 dropsondes launched during the eight research flights (Klepp et al. [2014]).

3.2 HALO Microwave Package (HAMP)

HAMP combines passive and active remote sensing in the microwave spectral region and, thus, offers the simultaneous measurement of both integrated cloud quantities as well as the cloud's vertical structure [Mech et al., 2014]. The method of combining active and passive measurements to obtain better precipitation and cloud retrieval results has been followed for many years and is implemented on research platforms such as the A-Train satellites (Stephens et al. [2002]), the Tropical Rainfall Measuring Mission (TRMM, Kummerow et al. [1998]), or the ground-based cloud observatory JOYCE (Löhnert et al. [2014]). HAMP was manufactured by Radiometer Physics GmbH (RPG) and is owned by the Max Planck Institute for Meteorology, Hamburg.

The active component of HAMP serves to retrieve the atmospheric columnar structure. A Doppler cloud radar operating at 35.563 GHz (MIRA-36, Melchionna et al. [2008], Mech et al. [2014]) was installed, reaching a sensitivity of -30 dBZ with an integration time of 1 second and a footprint size of 130 m at a height of 13 km with 220 m/s ground speed.

The passive part of HAMP consists of three radiometer modules measuring brightness temperatures in 26 channels from 22 up to 200 GHz. The channels are selected in a way that they cover the four main absorption complexes by water vapor and oxygen in this range: seven channels around both the water vapor absorption complex at 22.2 GHz (K-band) and 183.3 GHz (G-band), and on the wing of the oxygen complex at 60 GHz (V-band), as well as four channels around the oxygen 118.75 GHz complex (F-band) and one window frequency at 90 GHz (W-band). Figure 3.3 shows the simulated brightness temperatures by the **P**assive and **A**ctive **M**icrowave radiative **TR**ansfer (PAMTRA) model in different frequencies for a clear and a cloudy atmosphere over the ocean, indicating the positioning of HAMP's channels in the spectrum. The cloud was simulated with an LWP of 1000 gm^{-2} between 1 and 2 km.

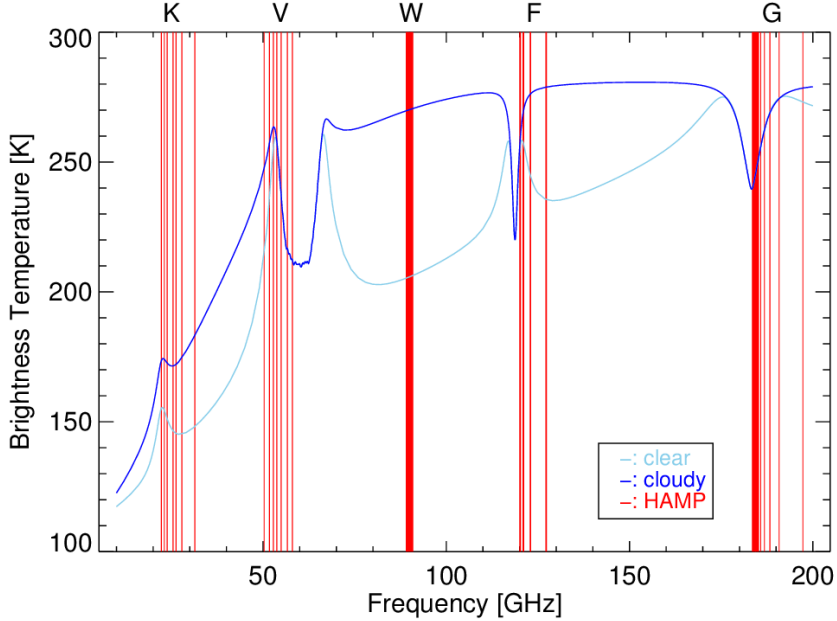


Figure 3.3 – PAMTRA simulated brightness temperatures between 10 and 200 GHz for clear (bright blue) and cloudy (dark blue) simulation. The cloud was simulated between 1-2 km holding 1000 gm^{-2} liquid water. HAMP’s channels are indicated in red with their respective channel width (see tab. A.1).

HAMP’s passive part is built in three modules. The two modules measuring in the K-,V- and W-bands are direct detection radiometers detecting and amplifying the received radiation directly at the receiving frequency. In addition to a pre-flight calibration using a liquid nitrogen and ambient temperature target, continuous gain-calibration is performed via Dicke switching to an ambient temperature target. The Noise equivalent Delta Temperature (NeDT), giving the internal noise error of the channels, ranges between 0.2 and 0.6 K (see tab. A.1).

The F- and G-band modules are based on the double-sideband heterodyne principle. The receiving signal is converted down to an intermediate frequency by a local oscillator before the amplification. After the pre-flight calibration using external targets, a continuous calibration during the flight is performed by receiving signals from a noise diode. This is done in viewing direction, except of the G-band module, which receives radiation from a target via a turnable mirror. This procedure can take up to 20s, leading to gaps in the T_B measurements in the G-band.

The half power beam width of the different bands ranges from 2.7° (G-band) to 5.0° (K-band). Respecting the moving of the aircraft, this leads to a ground-resolution of approximately $1.42 \text{ km} \times 1.2 \text{ km}$ for the K-band at 14 km flight altitude

(see fig. 3.4). In addition to radiation originating from this footprint, sidelobe contributions of smaller than -30 dBc (-20 dBc for the G-module, respectively) impact the observed signal. Further instrument details can be found in table A.1.

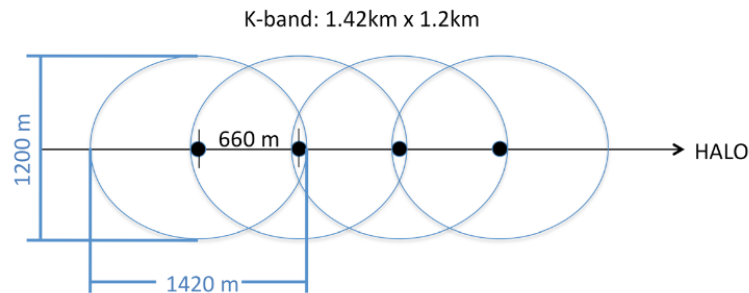


Figure 3.4 – HAMP footprint, 1.42 km x 1.2 km in size, of the K-band channels at a flight altitude of 14 km with a ground speed of 220 m/s at a 3 second sampling.

The 26 frequencies combine the channels selected on satellite instruments like the **A**dvanced **M**icrowave **S**canning **R**adiometer-**E**arth Observing System (AMSR-E) or SSMIS and offers a high potential to derive cloud properties from the measurements (Mech et al. [2014]).

Humidity and liquid water can be retrieved using the information of the K- and W-band channels, humidity and temperature profiles can be deduced including information from F- and V-channel (see sec. 2.3). Ice- and snowfall properties can be retrieved from higher frequencies such as in the G-band due to increased ice scattering (Mech et al. [2014]).

An example performance of HAMP’s passive and active parts is shown in figure 3.5, depicting the measurements during research flight RF06, 16.12.2013. HALO flew eastwards, taking off at Barbados at 13:10 UTC and landing at Oberpfaffenhofen, Germany, at 23:00 UTC. The brightness temperatures in the channels close to the absorption complex’s centers increase when a cloud enters HAMP’s field of view. The shift of the signal between 20:30 UTC and 21:30 UTC is due to land masses which have a higher background emissivity than the ocean surface. These features, as well as changes in flight altitude, impact the observations at the start and end of the flight. The change of height of the background clutter signal around 18:10 UTC is due to a change of flight altitude. The majority of the clouds detected by the radar in the tradewind region have cloud tops of not higher than 2 km above ground level. Precipitating clouds are sensed if the radar reflectivity signal reaches from cloud top down to the ground.

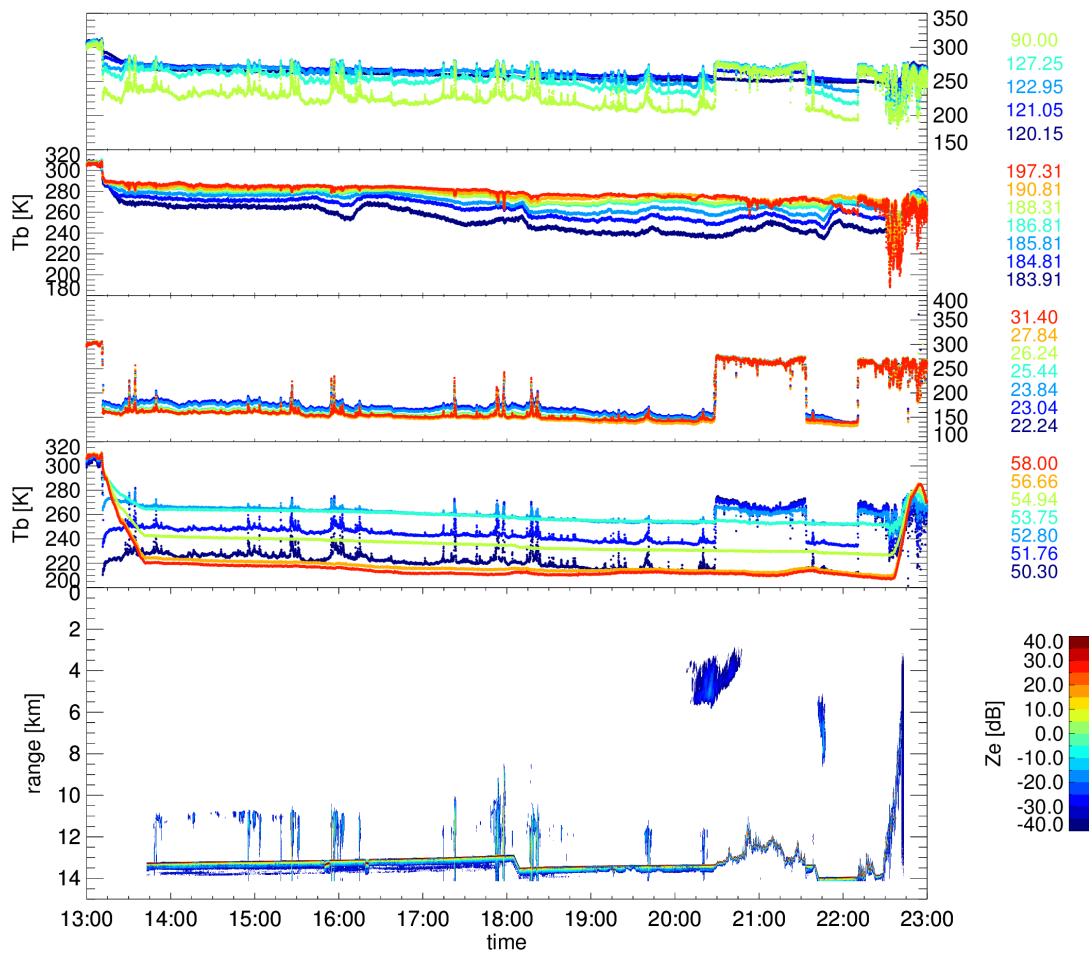


Figure 3.5 – HAMP raw measurements during research flight RF06, 16.12.2013, depicted as a function of time UTC. The measured brightness temperatures in the different bands are shown in the upper four panels. The radar signal is displayed in the lowest panel. The altitude scale is inverted such that 0 km refers to HALO’s altitude.

4 Airborne derived cloud properties

The following chapter will describe and analyse the derivation of macrophysical cloud properties from airborne data measured during the NARVAL South campaign. The following section 4.1 will treat the derivation of vertical integrated properties, such as the **Liquid Water Path (LWP)** and the **Integrated Water Vapor (IWV)**, derived from HAMP passive radiometric measurements. In section 4.2, the potential of the sensor synergy installed on HALO will be described and exploited to derive horizontal cloud properties such as the size distribution of the observed clouds.

4.1 Vertically integrated properties

In this subsection, the vertical integrated properties IWV and LWP will be derived using the HAMP passive radiometer measurements. First in section 4.1.1, the used algorithm to retrieve information about the quantities will be described and tested in respect to its sensitivity to the assumed radiometric brightness temperature errors and the **Sea Surface Temperature (SST)**. In the following subchapters, the retrieved IWV and LWP will be evaluated. For IWV, section 4.1.2 will discuss the derivation of a bias-correction term to account for missed IWV in the layers above HALO. The retrieved IWV uncertainty will be derived from the comparison to independent IWV measurements obtained from launched dropsondes. Based on this evaluation, the optimal choice of frequencies used in the retrieval will be developed. The LWP retrieval will be analysed in section 4.1.3. First, a clear-sky offset correction will be developed and the lowest resolvable LWP value will be derived. The clear-sky offset corrected LWP will be compared to the LWP retrieved from HALO-SR radiation measurements.

4.1.1 HAMP Retrieval Development and Sensitivities

In order to retrieve information about cloud properties from HAMP radiometric measurements, a statistical retrieval developed by E. Orlandi (personal communication) is applied to the data. Statistical retrievals cover all varieties of cases

which can occur in measured situations. They are based on a database with known atmospheric states and brightness temperatures at various frequencies, from which the coefficients of the retrieval function can be developed and, then, applied to the measured brightness temperatures to obtain atmospheric parameters. In this work, the retrieved atmospheric properties are restricted to IWV and LWP. Combining the data with profiling measurements like the lidar offers the potential to retrieve humidity profiles (Barrera-Verdejo et al. [2016]). The development of the HAMP retrieval is further explained in the next paragraph and summarised by figure 4.1.

The HAMP retrieval database is built upon about 10,000 entries based on the 75 dropsonde observations throughout the campaign. The measured temperature and humidity conditions are combined with 23 synthetic clouds with different LWP values in six different cloud height bins up to 3 km. The boundary of 3 km was chosen as in the tradewind region, clouds are not assumed to be at higher altitude (see sec. 2.1). The distribution of the LWP values in the database was chosen such that the occurring distribution of LWP in the tradewinds is respected, but also a large range of LWP is covered.

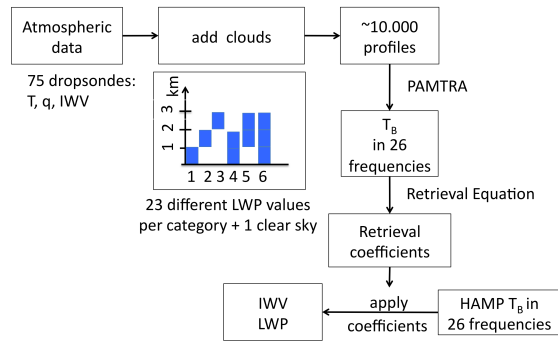


Figure 4.1 – LWP and IWV statistical retrieval strategy.

For each of the database entries, i.e. for each atmospheric state, a brightness temperature was simulated in each HAMP frequency using the **P**assive and **A**ctive **M**icrowave **T**RANSfer model (PAMTRA). Following the strategy described in Crewell and Löhnert [2003], a random normally distributed noise around each channel’s absolute brightness temperature error (see tab. A.1) is added to the simulated brightness temperature to simulate a real measurement. The IWV and LWP retrieval relies on a quadratic retrieval approach as suggested by Löhnert and Crewell [2003] (see eq. 4.1.1 with q_{ret} either IWV or LWP). The SST is included to provide information about the background emission and is derived from a daily resolved dataset on a $0.25^\circ \times 0.25^\circ$ grid, developed by Reynolds et al. [2007].

$$q_{ret} = a + \sum_{i=0}^{n_{freq}} b_i \cdot T_{B_i} + \sum_{i=0}^{n_{freq}} c_i \cdot T_{B_i}^2 + d \cdot SST \quad (4.1.1)$$

We can derive the retrieval coefficients a , b , c and d for various frequency combinations by applying a multi-linear regression to the simulated data and their corresponding atmospheric parameters. When retrieving IWV and LWP from the HAMP measurements, all brightness temperatures T_{B_i} from the channels used in the retrieval are first put on the same time resolution. While combinations including the G-band channels have lower time resolution and gaps due to calibration (see sec. 3.2), retrievals not including these channels offer a time resolution of about 2 to 3 seconds.

Then, the measured brightness temperatures are bias-corrected by the mean of the simulated measurements per flight (E. Orlandi). The retrieval result for IWV and LWP is obtained by applying the retrieval coefficients to the corrected measured brightness temperatures and corresponding SST. As the regression finds the coefficients by minimizing the sum of squared residuals, unphysical negative LWP values can result, especially in clear-sky cases (see e.g. Horváth and Gentemann [2007]). These are kept in the further analysis in order to not impact the distribution of the retrieved LWP.

The performance of the retrieval values can be evaluated by comparison to independent measurements assuming to measure the "true" atmospheric state. This will be performed for IWV in section 4.1.2. Due to the lack of comparison possibilities for LWP, the evaluation of the LWP retrieval performance is based on clear-sky cases (see sec. 4.1.3).

The accuracy of the retrieval assumptions also influence the uncertainties associated with the retrieval results. Precipitation and clouds higher than 3 km are not assumed in the statistical database, and will, thus, lead to uncertainties in the retrieved values in these situations. Additionally, model errors, such as the assumed droplet size distribution, the implemented absorption model, and background emissivity calculations will contribute. These error sources are summarised in the theoretical retrieval error.

An accepted strategy to approximate the theoretical retrieval error is to divide the database into two parts, a training data set and a test dataset. The training

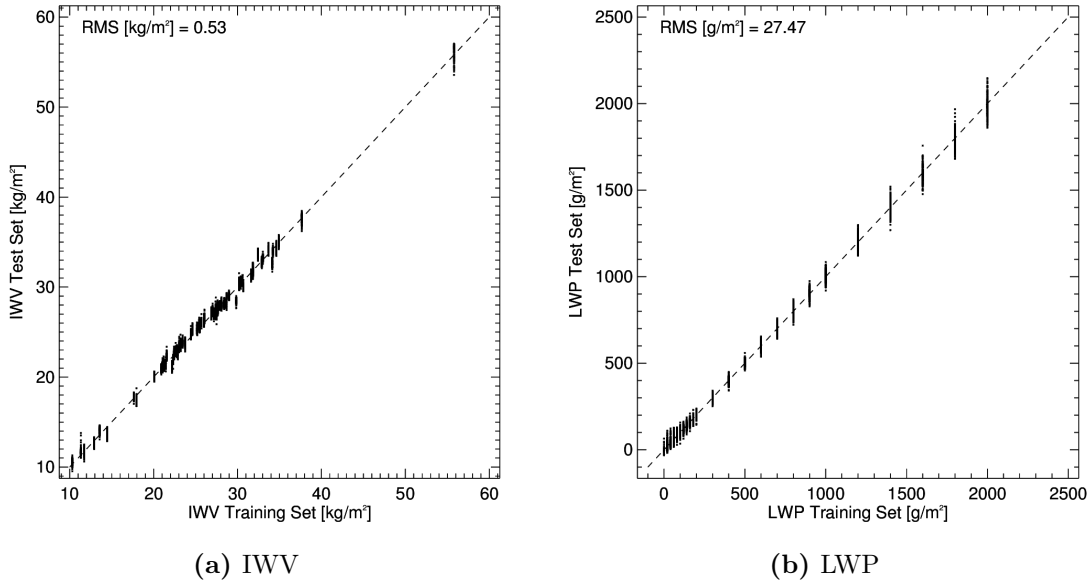


Figure 4.2 – Comparison of simulated training set to retrieved test set results with each 5073 entries. The theoretical error equals the RMS and for IWV computes to 0.53 kgm^{-2} , for LWP to 27.47 gm^{-2} , respectively.

dataset is used to derive the retrieval coefficients which are then applied to the test dataset. By comparing the simulated LWP and IWV from the training set to the retrieved LWP and IWV from the testset, the resulting **Root Mean Square (RMS)** error will represent the theoretical retrieval error. When applying this method, it is important that both datasets statistically cover all occurring possibilities with a satisfying number of cases (see Löhnert and Crewell [2003]). Figure 4.2 depicts the results of the strategy, here applied to the brightness temperatures of the seven K-band channels and the window-channel at 90 GHz, forming a database of 10146 situations, which is then divided into two sets. The resulting theoretical retrieval uncertainty for IWV sums up to 0.5 kgm^{-2} , for LWP to 27.5 gm^{-2} .

In order to derive the sensitivity of the retrieval algorithm to the assumed errors per HAMP channel and the SST, the variations of the theoretical retrieval RMS were analysed by varying the parameters under investigation. These tests were performed for various frequency combinations. In the following, the results of the channel combination of all K-band channels and the 90 GHz channel will be presented.

The sensitivity of the retrieval to SST was tested in a first experiment by analysing the impact of excluding SST from the retrieval, developing new coefficients, and comparing the resulting theoretical retrieval RMS to the standard retrieval approach (see fig. 4.3).

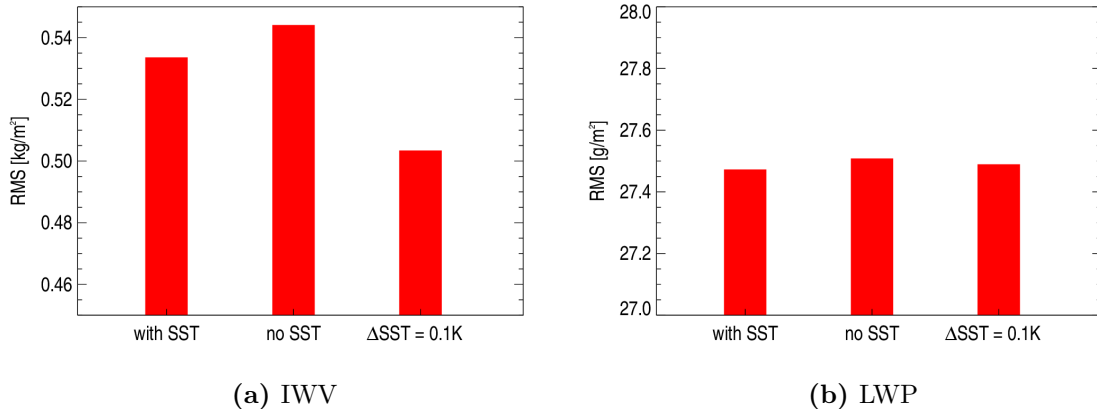


Figure 4.3 – Retrieval Sensitivity to SST. The theoretical RMS was calculated for including SST with an associated uncertainty of 2 K, excluding SST from the retrieval equation, and including SST with an error of 0.1 K.

The addition of SST with an assumed error of $\Delta\text{SST} = 2\text{ K}$ improved the RMS error by 2% for IWV and hardly made any impact for LWP. This confirms the expectations as evaporation from the ocean surface, depending on the temperature of the ocean water, determines the amount of atmospheric water vapor. Forcing the retrieval to rely more on the SST term by lowering the associated SST uncertainty, led to a decreasing RMS. Due to the low sensitivity of the algorithm to the SST dataset and the decrease in RMS when forcing the retrieval to rely on the SST, the HAMP measurements offer the potential to retrieve SST.

In a second test, the sensitivity of the quadratic retrieval including the SST term to the associated absolute T_B errors was tested by doubling the absolute T_B error in different channels (see absolute errors in tab. A.1).

As expected, the RMS in IWV and LWP increases when all measured T_B s have doubled uncertainty. Referring to figure 4.4, the channels on which the retrieval relies the most on, can be derived. When retrieving IWV, the information contained in the K-band, and therein, the 23.84 GHz channel, have the highest impact on the IWV. This confirms theoretical expectations as the K-band is sensitive to water vapor absorption and emission, and has a height independent weighting function. When retrieving LWP, the window channels at 90 GHz and 31 GHz add most of

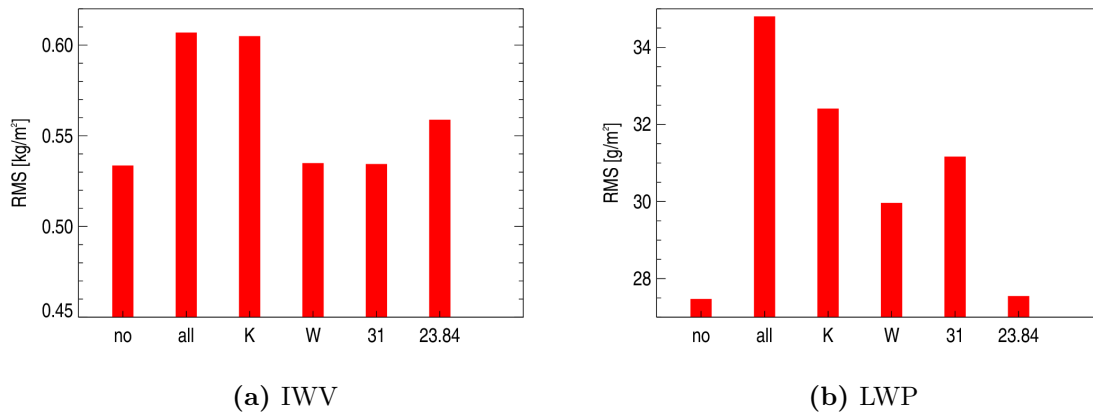


Figure 4.4 – Retrieval Sensitivity to the associated T_B error with SST included in the retrieval. As a function of the denoted band, the corresponding absolute error, assumed to equal the NeDT, was doubled.

the information content to the retrieval. The 31 GHz channel seems to be more sensitive to LWP which was not expected as liquid water absorption increases with the frequency squared. This result, however, might be impacted by the fact that the absolute error was doubled. This would increase the relative error in the lower frequency channel to a higher amount than in the 90 GHz channel.

4.1.2 I WV Retrieval Evaluation

During the campaign, HALO flew at an average altitude of 13 km. The retrieved values of I WV and LWP, thus, only represent the properties of the underlying column. As HALO overpassed cloud scenes, the retrieved LWP represents the entire column value as for example observed from space. Depending on the latitude, the tropopause shifts in altitude and might lie above HALO. Thus, water vapor can still be present above HALO which would lead to an underestimation of the retrieved I WV value compared to the corresponding observation from space.

In order to quantify the amount of moisture above the average flight altitude as a correction term for comparisons to satellite data, the profiles of radiosondes launched from Grantley Adams Airport, Barbados, were evaluated for each flight day. Thereby, it is assumed that the radiosondes ascended vertically and that the climatological situation over Barbados is representative for the entire tradewind driven region. The measurements give information about the temperature, relative humidity and mixing ratio at specific heights throughout the ascent. Calculating the absolute humidity

and vertically integrating through the column gives an estimate of the moisture, i.e. IWV, above and underneath 13 km as seen in figure 4.5.

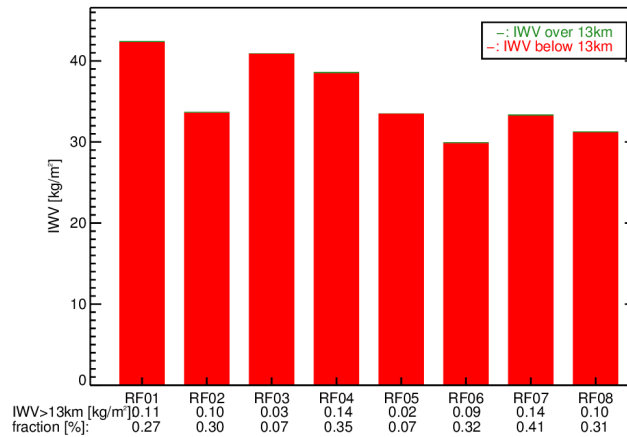


Figure 4.5 – Estimation of IWV amount from the parts of the vertical column above HALO at a flight altitude of 13 km. Its relative amount did not exceed 0.5 %.

During the eight flight days of NARVAL South, the relative amount of IWV above 13 km does not contribute more than 0.5 % to the total column IWV. As north-eastern winds prevail in this region, the radiosondes horizontally drift southwestwards into deeper tropical regions with a higher tropopause and increased humidity in high altitudes compared to the subtropics (Roedel [2000], p 76). Additionally, radiosondes experience measurement problems once reaching the stratosphere, with increasing uncertainties assigned to the humidity measurements. Therefore, the uncertainty of the correction term is assumed to be higher than the error introduced by HAMP not observing the total column. Thus, the retrieved IWV values are assumed to be representative for the entire column.

The uncertainty of retrieved IWV can be derived by comparison to independent measurements capturing the same situation. For IWV, the launched dropsondes can be exploited to evaluate the retrieval performance. It is assumed that the dropsondes did not experience horizontal drifting and that they measured the "true" atmospheric state in the scene below HALO. Figure 4.6 shows a performance example, taken from research flight RF08, 20.12.2013, at 19:25 UTC.

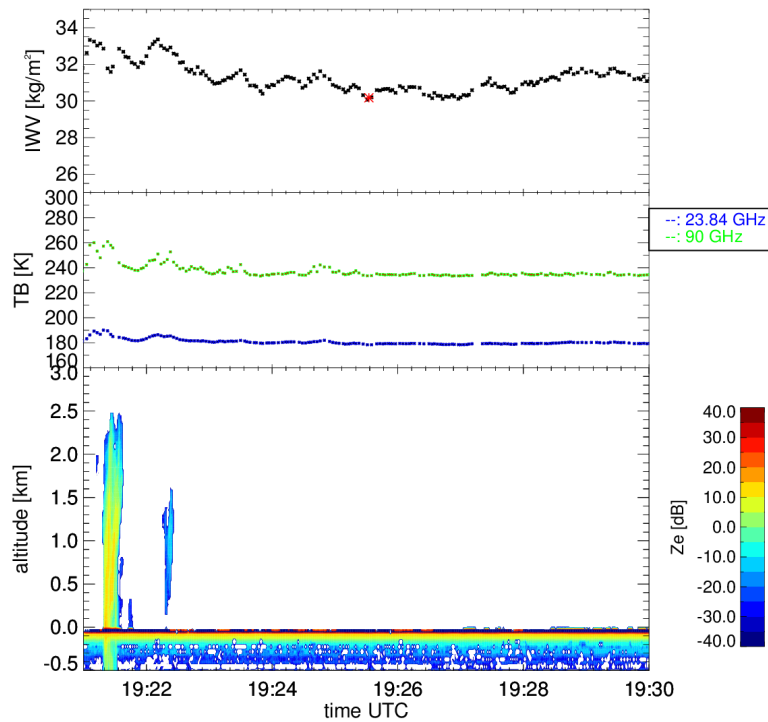


Figure 4.6 – Performance example between dropsonde and HAMP derived IWV, taken from research flight RF08, 20.12.2013, 19:25 UTC. Shown is the retrieved IWV (black) from HAMP and the dropsonde IWV (red asterisk) in the upper panel. The middle panel shows the observed brightness temperatures in the 23.84 (blue) and 90 GHz (green) channels. The radar profiled reflectivity is shown in the lowest panel.

The retrieval IWV matches the dropsonde IWV perfectly in this clear-sky case. In this scene the retrieved IWV lies within the range of IWV found by Trenberth et al. [2005] who estimated the subtropical IWV between 30 and 40 kgm^{-2} .

When expanding the analysis to all available dropsondes during the campaign, an average value of HAMP IWV was calculated within 30 seconds around each dropsonde launch point, assuming that the IWV conditions did not change significantly within this time period. The retrieval results using information from all K-band and the 90 GHz channels are compared with the dropsonde measurements as shown in figure 4.7.

The dropsondes launched during the flights which only covered the region east of Barbados (RF02 - RF05) all lie within an IWV of 20 to 35 kgm^{-2} . These results are lower than the values found by Trenberth et al. [2005] because NARVAL took place in the dry winter season, whereas Trenberth et al. [2005] uses a year average value in his analysis. The points outside of this range all originate from the transatlantic

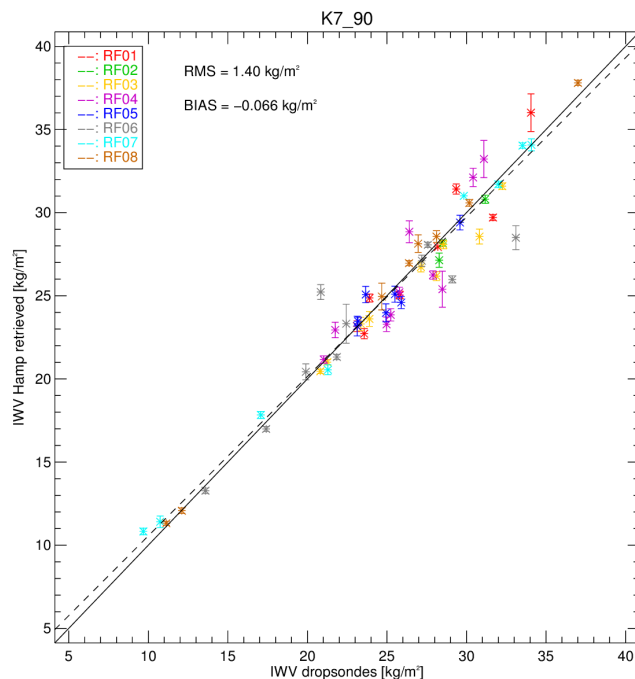


Figure 4.7 – Comparison of HAMP retrieved IWV to dropsonde IWV measurements, indicating the research flight in different colors. The errorbars associated to the HAMP measurements represent the standard deviation of IWV within the 30 second period around each dropsonde launch. The resulting RMS computes to $\text{RMS} = 1.40 \text{ kgm}^{-2}$ with a bias of $\text{RMS} = -0.07 \text{ kgm}^{-2}$.

flights. IWV below 20 kgm^{-2} was measured at higher latitudes where the atmosphere contains less water vapor. The linear regression of HAMP IWV and dropsonde IWV gave $\text{RMS} = 1.40 \text{ kgm}^{-2}$ with a bias of -0.07 kgm^{-2} . Compared to the observation range of IWV, this bias is negligible in further analyses.

This comparison can be expanded to different band combinations to find the channel combination leading to the least uncertain retrieval result, as depicted in figure 4.8.

The standard groundbased retrieval approach developed by Westwater [1978] uses information from an absorbing line in the 22.2 GHz water vapor absorption complex in combination with a window channel at 31 GHz to retrieve IWV. Using the observations in the 22.23 GHz channel in combination with the 31 GHz channel leads to an RMS of 1.54 kgm^{-2} , whereas combining 31 GHz information with the 23.84 GHz measurements led to an increase in RMS by 5 % to 1.62 kgm^{-2} .

Adding the additional five K-band channels to the retrieval (K7) decreases the RMS by 7%. Theoretically, a decrease of RMS is expected by adding more information from other channels to the retrieval. However, similar to ground-based results by

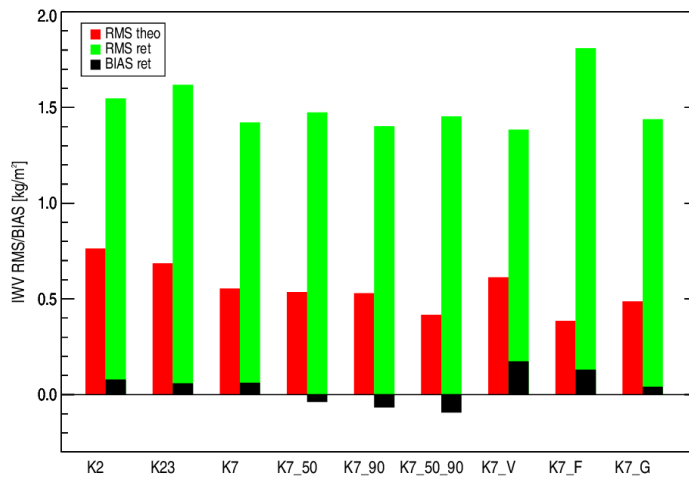


Figure 4.8 – Results of the evaluation of HAMP retrieved I WV values with independent dropsonde I WV measurements using different channel combinations in the retrieval. Shown are the theoretical retrieval RMS (red) obtained by the method introduced in fig. 4.2, as well as the RMS (green) and bias (black) derived from comparing HAMP and dropsonde measurements. The combination of K-band channels with 90 GHz channels led to the most reliable channel combination.

Löhnert and Crewell [2003], the addition of information from the 50 GHz channel (K7+50) or the 50 and 90 GHz channels (K7+50+90) increases the RMS slightly compared to only considering K-band channels. Adding the measurements of the 90 GHz channel (K7+90) lowers the RMS to 1.40 kgm^{-2} .

If channels from the V-band are added (K7+V), a significant bias increase can be observed compared to K7+90 even though the RMS is the smallest observed. Adding information from all four F-band channels to the K-band measurements (K7+F) has the lowest theoretical retrieval error, but introduces higher uncertainties than the K7+90 combination in the comparison to dropsonde I WV, indicating a calibration problem. The RMS of the combination of K- and G-band is only by 3% higher than the K7+90 combination, which offers potential for applications in ice-clouds.

The channel combination of all seven K-channels and the 90 GHz channel, leading to the most accurate I WV retrieval, is also suitable for the LWP retrieval, as figure 4.9 shows. As no independent measurements are available, the theoretical retrieval errors are depicted for the same band combinations as before.

The analysis confirms that exploiting all K-band channel information also reduces the theoretical RMS significantly by more than 15% compared to the two-channel

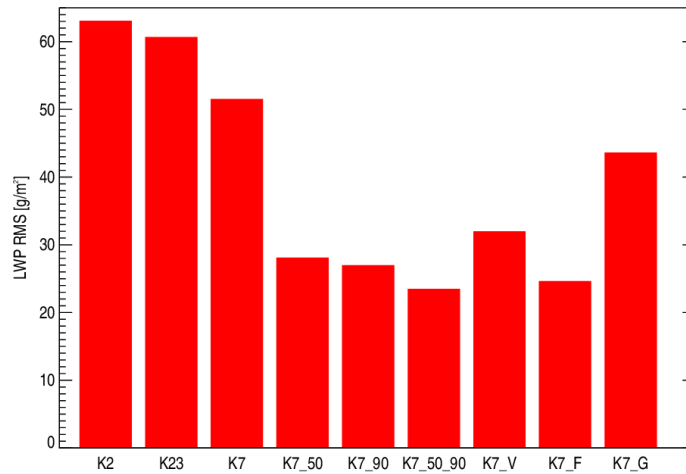


Figure 4.9 – Theoretical LWP RMS derived for different channel combinations by the method introduced in sec. 4.1.1.

retrievals. For LWP, only the addition of 50 GHz and 90 GHz and the addition of all F-band channels lead to a lower RMS. The IWV uncertainty, however, increases for band combinations with 50 GHz or F-band channels. Therefore, the retrieval of IWV and LWP based on the brightness temperature observations in all seven K-band channels and the 90 GHz window channel will be applied to the observations for further analyses. The comparison to independent dropsonde data assigned an uncertainty of $\text{RMS} = 1.40 \text{ kgm}^{-2}$ to the IWV retrieval result.

4.1.3 LWP performance analysis

An uncertainty estimation of the measured LWP based on independent measurements results is not possible due to the lack of reliable observations by other instruments. Therefore, the lowest detectable LWP is derived by analysing clear sky conditions similar to the approach described in Löhnert and Crewell [2003]. These scenes are identified using the 90 GHz channel by calculating the standard deviation of the signal within 30 seconds. If this standard deviation is below a certain threshold, the scene is identified as clear, and the clear sky LWP is set to the average LWP within the 30 second long period.

Due to noise in the measurements and uncertainties in the retrieval, the retrieved LWP is not always 0 gm^{-2} but is normally distributed around this value. In order

to account for this offset, van Meijgaard and Crewell [2005] suggest to subtract the nearest observed clear-sky LWP from each HAMP measurement. This method reduces the amount of negative retrieval results and shifts the center of the LWP distribution to approximately 0 gm^{-2} . Gaussiat et al. [2007] exploit the synergy of radiometer and lidar ceilometer to detect clear-sky periods and set the retrieved clear-sky LWP to 0.

In this study, only radiometer data was used to identify clear-sky scenes, assuming that in clear-sky situations, the standard deviation of the 90 GHz-channel within 10 measurements around each measurement point did not exceed a certain threshold. This threshold T_{Bt} was investigated by identifying clear-sky scenes by eye, resulting in $T_{Bt} = 0.5 \text{ K}$, 0.1 K higher than the NeDT of 0.4 K of this channel (see tab. A.1). In order to exclude homogeneous clouds with small variability in the W-band observations, derived clear sky points with more than 50 gm^{-2} were not considered. The clear-sky LWP for each clear-sky measurement was derived by taking the average LWP over the 10 neighboring measurements.

During all flights, 1,431 measurements were identified as clear-sky scenes which roughly make 2.6% of the total number of measurements during the campaign. The LWP in these scenes is assumed to be Gaussian distributed as shown in figure 4.10.

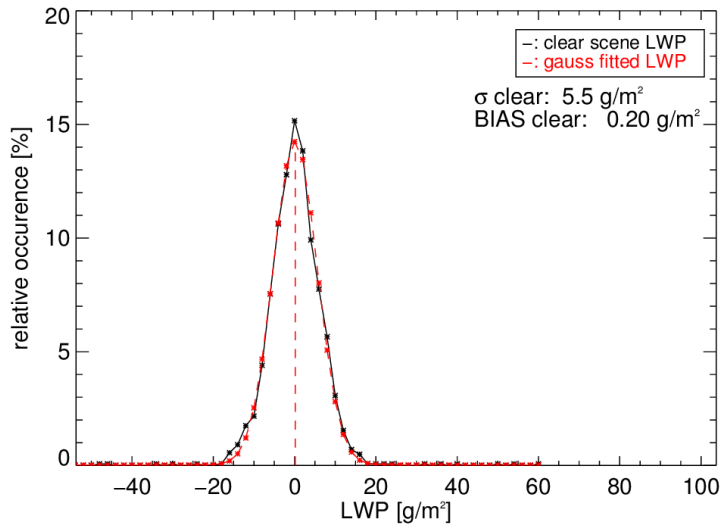


Figure 4.10 – HAMP retrieved LWP distribution (black) in clear-sky cases identified by a standard deviation threshold in the 90 GHz observations, binned to 2 gm^{-2} . A Gaussian fit (red) led to a standard deviation of $\sigma = 5.5 \text{ gm}^{-2}$ with a mean $\mu = 0.2 \text{ gm}^{-2}$.

The fitting of the distribution to a Gaussian function gave a standard deviation of 5.5 gm^{-2} with a mean value of 0.2 gm^{-2} . As the relative error introduced by the bias

is small compared to other error sources, it will be negligible in the following. Thus, in clear-sky cases, the LWP detection threshold is $\Delta\text{LWP} = 5.5 \text{ gm}^{-2}$.

All measurements were clear-sky corrected by deducting the closest clear-sky LWP measurement in time, which resulted in a change of LWP distribution as shown in figure 4.11. 3.4% of the total data lie beyond the ranges shown in the figure, but are included in the normalisation of the curve as they contribute to the total of the measurements.

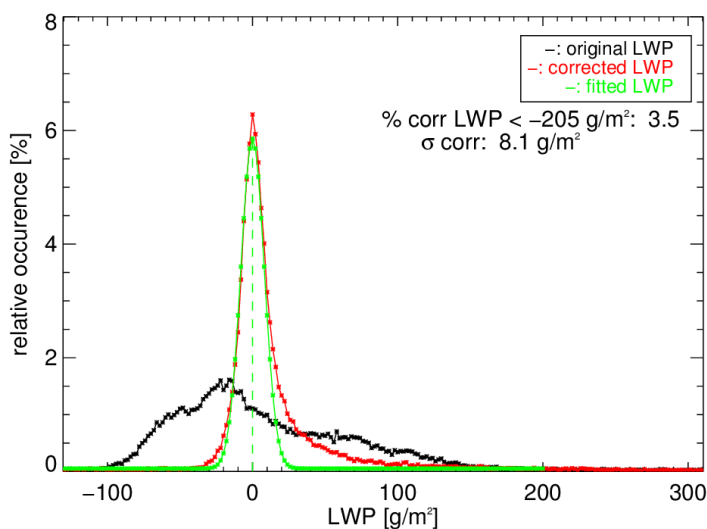


Figure 4.11 – HAMP retrieved LWP distribution, binned in 2 gm^{-2} steps, of the original retrieval result (black) and after applying the clear-sky bias correction (red), not including data below -200 gm^{-2} . A Gaussian fit with the mean centered at 0 gm^{-2} revealed a standard deviation of $\sigma = 8.1 \text{ gm}^{-2}$.

After the clear-sky correction, the amount of negative retrieval values is reduced by 8.45% to about 38%. These values are shifted to the positive LWP range with up to 100 gm^{-2} . In the calculation of the size of the first confidence interval, only the left wing of the bell curve with $\text{LWP} = 0 \text{ gm}^{-2}$ or negative LWP values was considered, as most of the clear sky measurements lie within this range. The resulting standard deviation of the Gaussian curve is 8.1 gm^{-2} , 47% higher than in only clear situations.

The difference between the two detection limits is thought to arise from the clear-sky detection approach. Additionally, the binsize used to present the data impacts the quality of the fit. Due to the semi-transparency of the atmosphere at the 90 GHz channel and the consequent sensitivity to changes in background emissions, errors are introduced in the clear sky detection approach. Clear cases where the ocean surface emissivity changed due to changes in ground wind-speed or SST can then

be erroneously identified as cloudy cases. This leads to an underestimation of all occurring clear sky cases, impacting the width of the distribution and, thus, the position of the first confidence interval.

In the following, however, the obtained detection threshold of $LWP = 8.1 \text{ gm}^{-2}$ is used to estimate the uncertainty associated to the retrieved LWP.

Independently retrieved data from HALO-SR (see sec. 3.1) is used to test the retrieval LWP performance. HALO-SR captures reflected solar radiation measured in six channels ranging from 422 to 1638 nm with 8% uncertainty and a time resolution of about 2 seconds (Fricke et al. [2014]). With a field of view of 2.1° and an integration time of 0.5 seconds, the data has a spatial resolution of 1 km^2 at a flight altitude of 14 km.

The reflected radiation measured at 650 and 1646 nm is used to retrieve optical depth τ and effective radius r_{eff} by matching the reflectances to the most accurate fitting combination of τ and r_{eff} following the approach developed by Nakajima and King [1990]. With τ and r_{eff} , LWP can be calculated with equation (2.3.2) with an accuracy of about 10% (personal communication André Ehrlich, University of Leipzig).

Limitations to the optical retrieval are introduced by the reflectivity of the over-passed surface, aerosol scattering, and the solar height. At low sun angles, 3D-scattering effects increase and lead to an overestimation of τ (Fricke et al. [2014]). Effective radius is retrieved from the $1.65 \mu\text{m}$ channel, where radiation has a low penetration depth into the cloud due to high absorption by liquid water (Platnick [2000]). Thus, as discussed in section 2.3, the retrieved effective radius only represents the droplets' size at the top of the clouds, which are assumed to be vertically homogenous distributed through the rest of the cloud. According to Borg and Bennartz [2007], this can lead to an underestimation of the "real" LWP for clouds containing more than 150 gm^{-2} . Due to these limitations in the retrieval, the HALO-SR data is not used as a reference to evaluate the microwave LWP retrieval, but for detecting clouds.

Before comparing the two datasets, the times still needed to be matched, as both instruments were connected to different machines. The absolute timestamp difference between the two datasets was derived by analysing the correlation between the radiance signal of the 422 nm and the brightness temperature at 90 GHz. One correction term was derived for each flight which varied between 4 and 7 seconds.

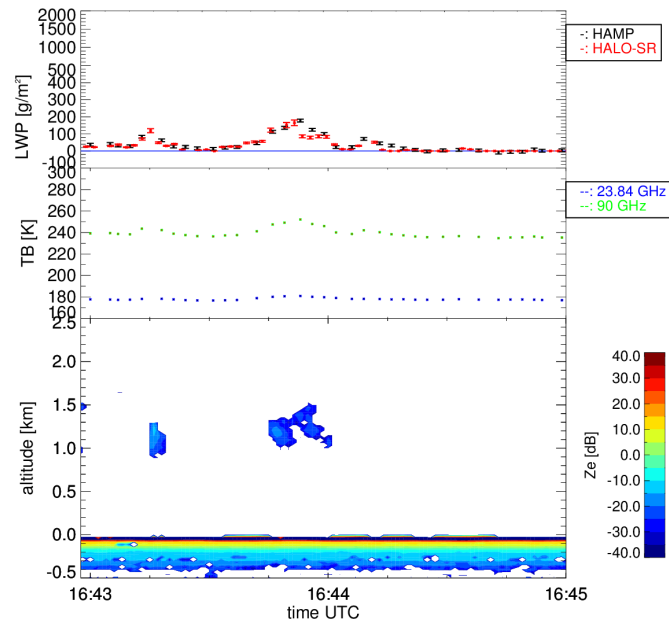


Figure 4.12 – Performance of HAMP active and passive part and coincident HALO-SR retrieved LWP during RF03, 13.12.2013, 16:43 - 16:45 UTC. The upper panel shows LWP retrieved from HAMP (black) and HALO-SR (red). The middle panel depicts the measured brightness temperatures of the 23.84 GHz (blue) and 90 GHz-channel (green). The radar reflectivity is shown in the lowest panel.

Figure 4.12 shows two shallow detected clouds with less than 200 gm^{-2} . For these non-precipitating shallow cumuli, the retrieval products agree nearly perfectly within the retrieval uncertainties. Cases where the radar observed deeper clouds or precipitation will be analysed in the next section.

4.2 Cloud Properties Exploiting Sensor Synergy

Additional cloud properties can be derived exploiting the different sensors mounted on HALO with their specific instrument characteristics. In section 4.2.1, the potential for the development of a precipitation flagging algorithm will be discussed, exploiting the potential of HAMP's active component, the MIRA-36 cloud radar. A cloud detection strategy (cloud mask) will be developed basing on radiance measurements of HALO-SR and applied to derive horizontal cloud properties such as cloud length and LWP in section 4.2.2. This information will lead to the derivation of climatological characteristics such as the cloud length- and LWP-length distribution.

4.2.1 Synergy potential

From section 2.3 we can recall that active sensors like HAMP's 35 GHz radar have a high potential to retrieve the structure of clouds, as the reflectivity factor Z depends on the hydrometeor's radius to the power of six (see eq. 2.3.1). Passive sensors like HALO-SR or HAMP's radiometer part give information about integrated vertical properties like IWV and LWP, based on the reflection of sunlight at the cloud tops in the first case, or microwave emission from the atmosphere and clouds in the second case. As already seen in section 4.1.3, the agreement between the two passive sensors in situations of non-precipitating, shallow clouds is satisfactory within the retrieval limitations.

Looking at the coincident performance of radar, radiometer and HALO-SR, however, more features can be derived giving a case example from research flight RF03, 12.12.2013, 16:00 - 16:15 UTC, depicted in figure 4.13.

Using the radar signal, precipitation cases can be identified with certainty when the columnar backscatter signal reaches down to the ground. This is the case right before 16:04 UTC showing a strong shower event, or before 16:03 UTC, with a weaker example. In both cases, the HALO-SR LWP retrievals underestimate HAMP's retrieved LWP. As discussed in section 4.1.3, this underestimation by the HALO-SR derived LWP due to the retrieval of effective radius from the cloud top and the lack of sensitivity of the instrument to the lower part of the cloud. Therefore, the radar can help to develop a precipitation flagging method to differentiate precipitating and non-precipitating cases. For the two different cases, retrievals for precipitation and non-precipitation can be developed. This knowledge can for example be used to

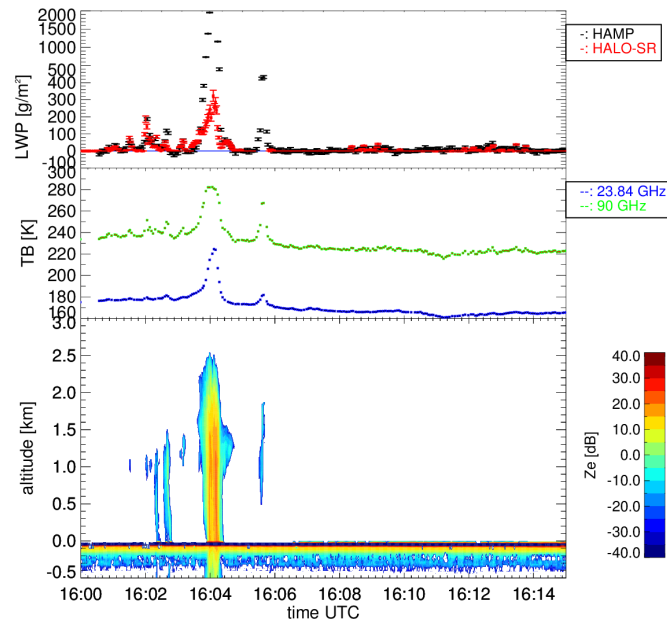


Figure 4.13 – Performance of HAMP active and passive part and coincident HALO-SR retrieved LWP during RF03, 13.12.2013, 16:00 - 16:15 UTC. The upper panel shows LWP retrieved from HAMP (black) and HALO-SR (red). The middle panel depicts the measured brightness temperatures of the 23.84 GHz (blue) and 90 GHz-channel (green). The radar reflectivity is shown in the lowest panel.

develop a microwave retrieval optimized for precipitation cases in order to decrease uncertainties in the LWP retrieval.

For small cumuli as for example at 16:01 UTC with about 80 gm^{-2} , the radar reaches its sensitivity limit with a backscatter intensity of -30 dB . Smaller clouds with a lower water content of about 50 gm^{-2} as between 16:00 and 16:01 UTC and 16:08 and 16:13 UTC are not captured by the radar.

In a case taken from RF03 at 16:42 to 16:45 UTC, similar characteristics can be derived as seen in figure 4.14.

The underestimation of the LWP in the HALO-SR optical retrieval can again be seen given the example of a cloud at 16:42 UTC, where HAMP measures an LWP of 100 gm^{-2} , twice as high as HALO-SR. From the radar signal, we can see that the reflectivity is not vertically homogeneously distributed, but increasing with distance to cloud top. The droplet size, in this case, increases with distance to cloud top, which leads to an underestimation of LWP derived from the Nakajima-King method (see eq. 2.3.2).

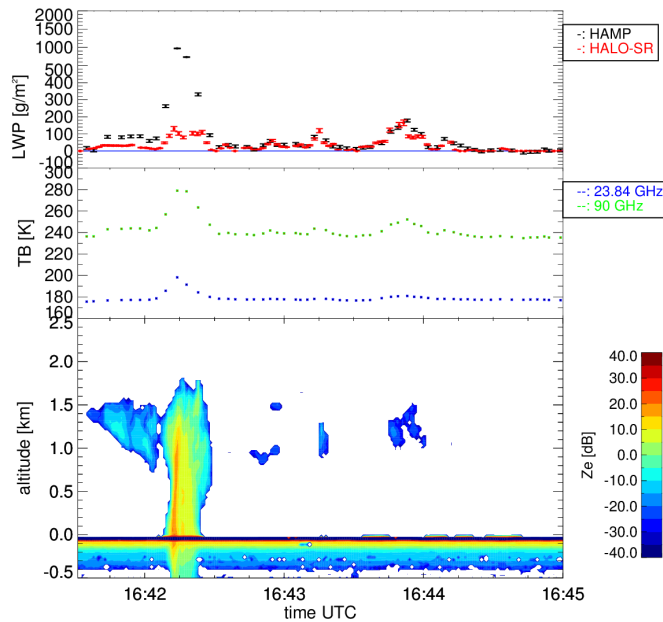


Figure 4.14 – Performance of HAMP active and passive part and coincident HALO-SR retrieved LWP during RF03, 13.12.2013, 16:42 - 16:45 UTC. The upper panel shows LWP retrieved from HAMP (black) and HALO-SR (red). The middle panel depicts the measured brightness temperatures of the 23.84 GHz (blue) and 90 GHz-channel (green). The radar reflectivity is shown in the lowest panel.

A second advantage of synergising the different sensors is the increased potential to identify cloud edges. As the radar signal misses thin clouds, we cannot rely on it in this case, but exploit the strong radiance gradient at cloud edges in the visible spectral range.

In figure 4.15, the same scene as in figure 4.13 is shown, this time also showing the radiance measurement by HALO-SR.

The missed clouds by the radar are clearly visible in the HALO-SR signal. The signal gradient at the edges of the clouds is stronger than in the brightness temperature signal. A physical explanation is given by the higher scattering efficiency of cloud droplets in the visible spectral range with respect to the microwave emissions. This result confirms the observations by Lin and Rossow [1994], who claim that optical measurements have a higher sensitivity to clouds and, thus, offer enhanced potential to develop a cloud mask algorithm.

Following the approach for MODIS described by Frey et al. [2008], a cloud mask algorithm has been developed from the HALO-SR data in this work. The algorithm assigns a clear or cloudy attribute to each measurement point depend-

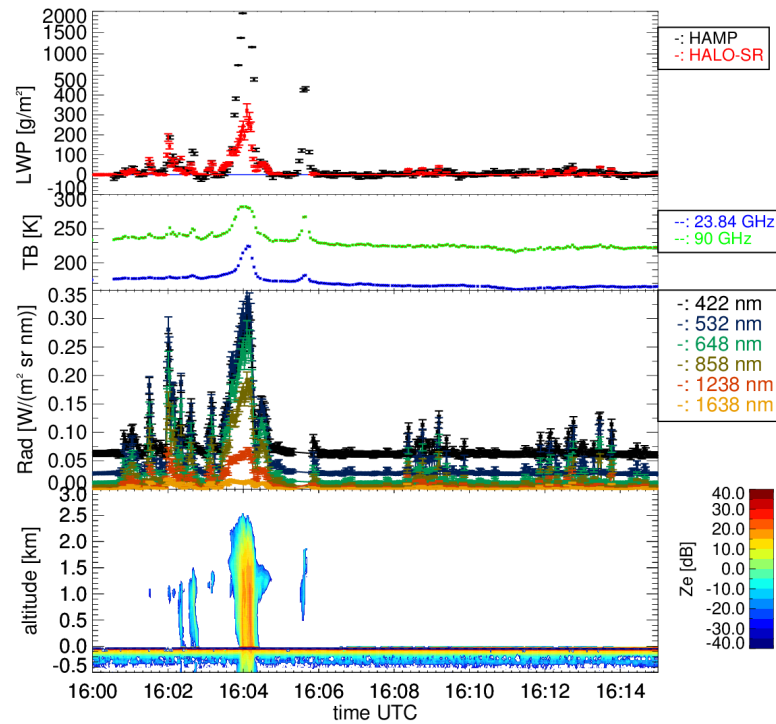


Figure 4.15 – Performance of HAMP active and passive part and coincident HALO-SR radiance measurements during RF03, 16:00 - 16:15 UTC. The upper panel shows LWP retrieved from HAMP (black) and HALO-SR (red). The middle panel depicts the measured brightness temperatures of the 23.84 GHz (blue) and 90 GHz-channel (green), as well as the HALO-SR observed radiance in six channels. The radar reflectivity is shown in the lowest panel.

ing on the observed radiances in the 648 and 858 nm channels. The attribute cloudy is set if the ratio and one of the two channels exceeded the thresholds of $\frac{\text{Rad}(858 \text{ nm})}{\text{Rad}(648 \text{ nm})} > 0.5$, $\text{Rad}(648 \text{ nm}) > 0.018 \text{ Wm}^{-2}\text{sr}^{-1}\text{nm}^{-1}$, or $\text{Rad}(858 \text{ nm}) > 0.01 \text{ Wm}^{-2}\text{sr}^{-1}\text{nm}^{-1}$. These thresholds were derived by expanding the example analysis performed by eye to an automatic detection algorithm for all available flight data.

The same example as in figure 4.15, where the edges of the clouds were analysed manually, is taken to present the performance of the cloud mask algorithm in figure 4.16.

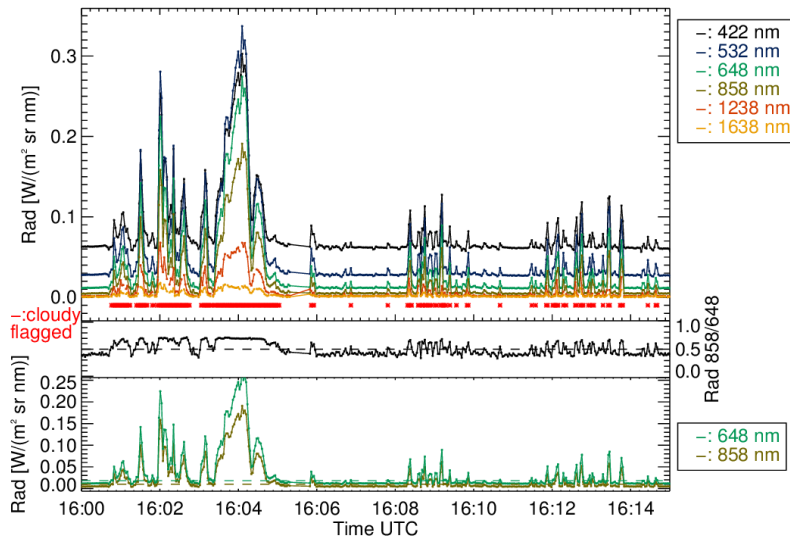


Figure 4.16 – Same case as in figure 4.15, giving an example for the cloud mask algorithm performance. The upper panel shows the radiance measured by HALO-SR in six different channels. The points flagged as "cloudy" are illustrated in red. The middle panel shows the ratio of the 648 to the 858 nm channel and the cloud mask threshold of 0.5. The lowest panel illustrates the measured signal in the 648 (green) and 858 nm (ocker) channels with the thresholds in the cloud mask algorithm of $0.01 \text{ Wm}^{-2}\text{sr}^{-1}\text{nm}^{-1}$ and $0.018 \text{ Wm}^{-2}\text{sr}^{-1}\text{nm}^{-1}$, respectively (dashed lines).

The cloud mask algorithm flags successfully all major appearing clouds. However, small features as for example at 16:10:30 UTC are missed. Lowering the detection thresholds, however, led to a flagging of clear scenes. For further applications, it might, thus, be feasible to develop thresholds for each flight as the instrument's performance and calibration changed from flight to flight.

4.2.2 Horizontal Cloud Properties

Using the cloud mask potential for further analyses, horizontal properties of the clouds can be derived based on the HALO-SR measurements. The edges of the clouds were derived by variation of the cloud mask attribute from clear to cloudy and vice-versa. The length of the clouds was calculated by deriving the time-difference between the edges of the cloud and multiplying it by the average ground-speed in that time period. Using this approach, 3808 clouds were detected during all NARVAL South flights.

When restricting the analysis to a typical tradewind driven region of 9°N to 20°N and 300°E to 320°E , still 3002 clouds were observed. Binning the observed cloud

lengths and normalising the number of counts per bin to the number of total clouds observed in all the cases and the trades, respectively, reveals very similar distributions for lengths up to 7 km in bins of 500 m, as shown in figure 4.17.

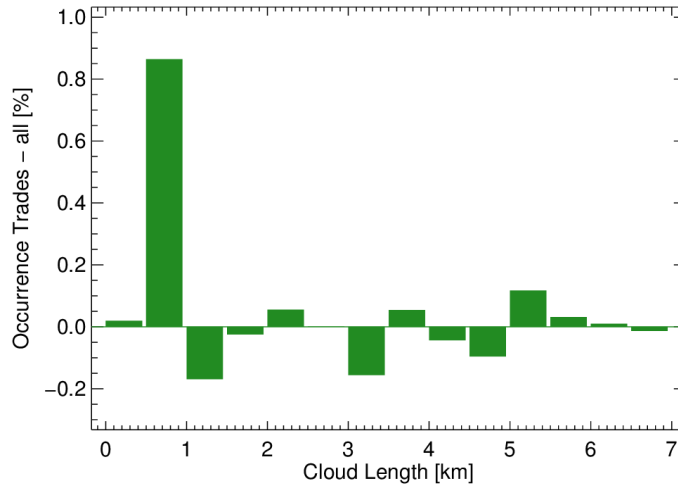


Figure 4.17 – Difference in the cloud length occurrence between a tradewind specific region and all observed clouds during NARVAL South for clouds with up to 7 km binned in 500 m bins. The distributions were normalised to the respective total number of observed clouds in the different considered regions.

Therefore, the following analysis is performed with the total number of clouds observed during the NARVAL campaign. The length distribution of those 3808 clouds is shown for lengths up to 7 km in figure 4.18.

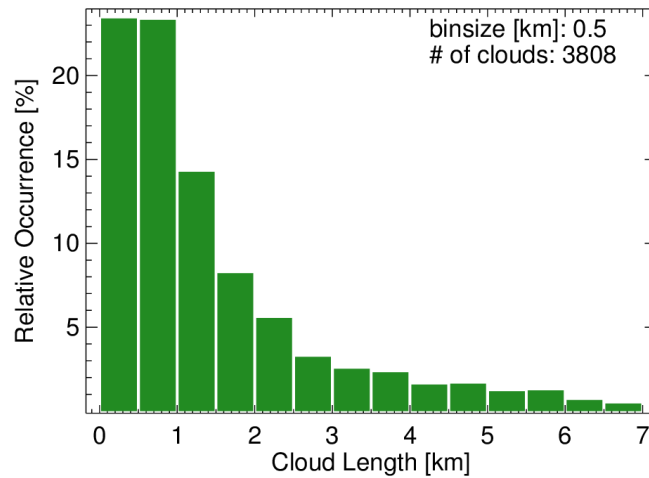


Figure 4.18 – Cloud Length Distribution for up to a cloud length of 7 km shown with a binsize of 500 m and normalised to the 3808 detected clouds during the campaign.

The maximum size occurrence is found in the bins ranging up to 1000 m, displaying about 46 %. Sixty-nine percent of all detected clouds are smaller than 2 km, 20 % more than observed by Zhao and Di Girolamo [2007]. This discrepancy can be introduced by the different resolutions of the datasets. Whereas the satellite data used by Zhao and Di Girolamo [2007] has a resolution of 15 m, the lowest detectable cloud by HALO-SR is 550 m in length when accounting for a field of view of 2.1° at a flight altitude of 14 km with the aircraft moving at a ground speed of 220 ms^{-1} .

Additional uncertainties are introduced by the cloud mask performance. As the detection algorithm may miss small clouds (see sec. 4.2.1), the length distribution is biased towards higher lengths. It is also not possible to resolve, where exactly the cloud started between the last clear and first cloudy measurement and vice-versa for the the cloud end, respectively. With an average sampling time of 2 seconds and an average groundspeed of 220 m/s, respecting the overlap of the footprint, this introduces uncertainties of 400 m at both edges of the cloud. Due to this uncertainty, gaps between clouds may be veiled and broken clouds captured as a single cloud, further adding towards the positive bias.

The exponent λ described in equation (2.1.1) can be derived by fitting the corresponding logarithmic function $\ln p(l) = \ln(a) - \lambda \ln(l)$ to the distribution plotted with double logarithmic axes. In this representation, the distribution follows a linear relation and λ can be derived by applying a least square fit to the data considering the bin center. The resulting linear regression fit is shown in figure 4.19 and revealed $\lambda = 1.72$.

The obtained value for the power-law exponent in equation (2.1.1) lies in the same range as observed by other studies (table 2.1). However, a direct comparison to these exponents cannot be performed as the shape of the cloud distribution depends on the binsize as described by Zhao and Di Girolamo [2007]. To overcome this limitation in comparison studies, the authors propose the "direct power-law" method, deriving λ by setting the mean to the expected value. This assumption is only valid for a "sufficiently large" sampling size. As their database contains one million entries, the number of clouds detected during NARVAL South is not considered to be high enough to apply their method.

For each of the derived clouds, a cloud LWP was derived by calculating the median of the HAMP LWP results within the cloud boundaries. However, 19 % of the detected 3808 clouds were too small to derive LWP as the HAMP measurements were performed less frequently than the HALO-SR measurements. The occurrence distribution of

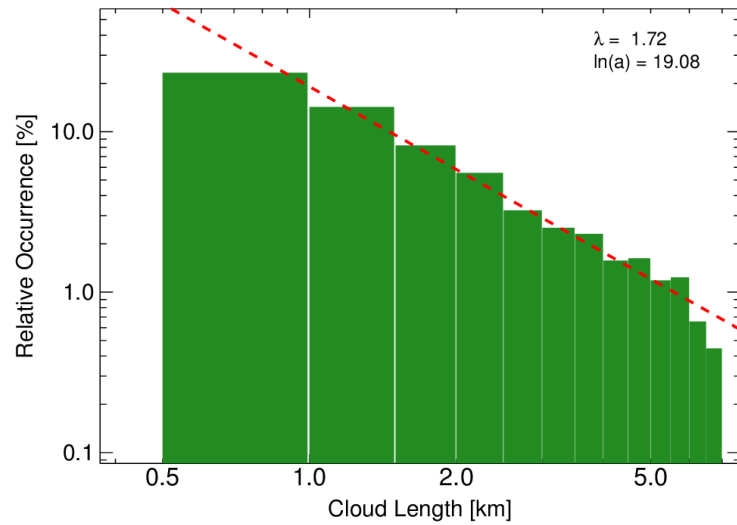


Figure 4.19 – Double logarithmic representation of the cloud length distribution with 500 m binsize. A linear regression gave the power law exponent $\lambda = 1.72$.

the different water contents of the resolved clouds is shown in figure 4.20. Yet, to be able to directly compare the values to the size distribution, the same basic amount of 3808 is used for normalization.

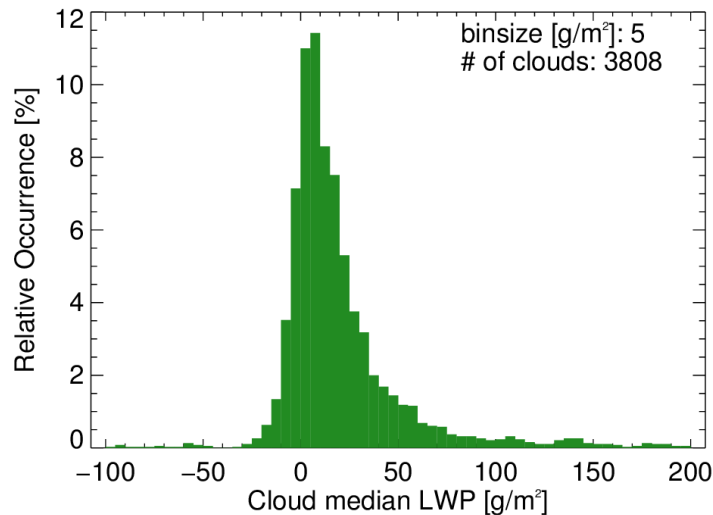


Figure 4.20 – Cloud LWP distribution binned to 5 gm^{-2} normalised to all detected clouds. The median LWP between the two cloud edges determined with the cloud mask algorithm was calculated.

The distribution peaks at an LWP close to 0 gm^{-2} . The total occurrence of clouds with an LWP higher than 200 gm^{-2} is 1.6%. About 46% of the observed clouds

contain less than 50 gm^{-2} . However, the calculation of the LWP per cloud depends on the cloud edge determination algorithm. The uncertainties associated with this also introduce an error in the LWP distribution. The exact quantification of this uncertainty still needs to be investigated.

Combining the derived cloud length and LWP distributions, the occurrence of clouds depending on both parameters can be investigated with the aid of figure 4.21. Even though about 10% of the sensed clouds were larger than 7 km, the analysis is restricted to clouds smaller than 7 km with LWP less than 500 gm^{-2} , assuming that precipitating clouds would contain a higher LWP. The occurrence of clouds per LWP and length bin is normalised to all available clouds.

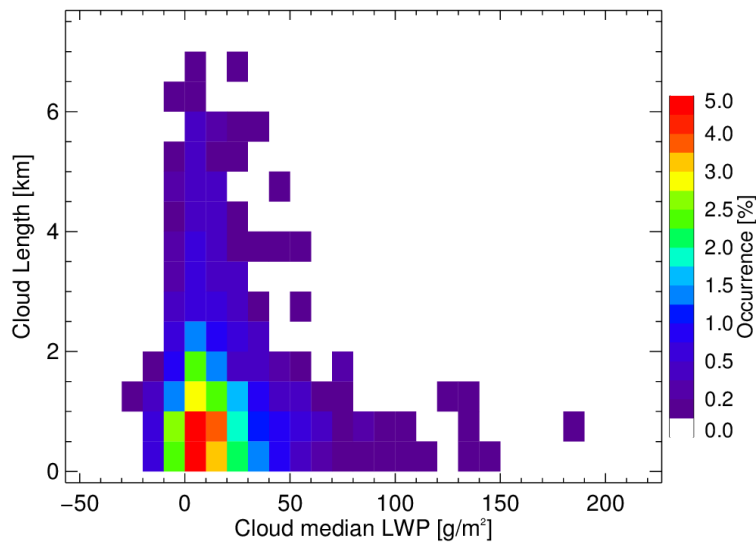


Figure 4.21 – Combined Length-LWP distribution. The occurrence is depicted in a corresponding color as a function of cloud median LWP binned to 10 gm^{-2} and cloud length in 500 m bins. The median LWP per length bin is illustrated as a black asterisk.

This representation confirms that about 70% of the clouds have a length smaller than 2 km. A majority of these clouds contain LWP of less than 50 gm^{-2} . Clouds with higher LWP than this appear only with less than 1% per bin. These obtained distributions can serve to evaluate LES modeling in the tradewind region as performed by e.g. Neggers et al. [2003b].

5 Satellite Product Evaluation

In the following chapter, the question will be discussed how coincident satellite measurements compare to the HAMP derived cloud properties, assuming that the airborne measurements represent the "truth". First, the observations of IWV and LWP by the **Special Sensor Microwave Imager/Sounder (SSMIS)** with a coarser resolution than the airborne measurements will be analysed in section 5.1. Moreover, the comparison of the LWP derived measurements by the **MODerate Resolution Imaging Spectroradiometer** with a similar resolution to HAMP's will be performed in section 5.2.

5.1 SSMIS IWV and LWP products

SSMIS and its IWV and LWP products will be described in the following section section 5.1.1. In section 5.1.2, starting from a case example, the comparison of coincident observations will be extended to all available direct overpasses. In section section 5.1.3, the statistical distributions of IWV and LWP derived from the two sensors will be compared in a typical tradewind region east of Barbados.

5.1.1 Data Description

The **Special Sensor Microwave Imager/Sounder (SSMIS)**, formerly **Special Sensor Microwave Imager (SSMI)** has been observing the Earth from space since 1987 embedded in the **Defense Meteorological Satellite Program (DMSP)**. These satellites are in a near-polar orbit from which SSMIS conically scans the Earth from a height of 833 km above surface with an angle of incidence of 53.4° (Wentz [1997]). It measures in 24 different channels from 19 to 183 GHz, and thus covers the K-, V-, W-, and G-band.

The retrieval algorithm applied to observed brightness temperatures was developed by Wentz [1997] to retrieve LWP, IWV, and surface-windspeed. The physical algorithm is based on information of the channels at 19, 22.23 and 37 GHz, with the former two sensitive to water vapor absorption, and the latter being a window

channel. The algorithm was further developed to retrieve rain rates by Wentz and Spencer [1998].

In the first retrieval step, the antenna temperatures are sampled to the antenna pattern of the 19 GHz observation, giving the brightness temperature in each channel with a cross-track resolution of about 56 km. Even though the instrument samples every 25 km, every measurement has a resolution of 56 km, which is the half power beam width the instrument receives radiation from.

Then, the set of retrieval equations is solved to best match the observed brightness temperatures to the corresponding LWP, IWV and windspeed. For rainy clouds, the algorithm is adapted to also retrieve rain rates. Wentz and Spencer [1998] state that in case of rainy clouds, the discrimination between cloud droplets and rain drops is not clear. Therefore, if observed LWP values are larger than 180 gm^{-2} , the cloud is considered to be precipitating and LWP is increased depending on the rain-rate. This correction is called cloud-rain partitioning (Wentz and Spencer [1998]).

Uncertainties in the retrieved products of IWV and LWP can arise due to assumptions in the absorption model used in the retrieval and the cloud-rain partitioning threshold (O'Dell et al. [2008]), and errors in the background surface emissivity calculation (Wentz [1997]). The lowest resolvable LWP is 10 gm^{-2} with a theoretically derived uncertainty of 25 gm^{-2} . IWV can be derived with an uncertainty of 1.2 kgm^{-2} (Wentz [1997]).

The data used in this work was measured by SSMIS on the satellite f16, provided by **R**emote **S**ensing **S**ystems (RSS, Wentz et al. [2012]). Gridded on a regular longitude/latitude grid of $0.25^\circ \times 0.25^\circ$, it provides retrieval products for both the morning ascending and evening descending orbit with equator passing times of 04:14 and 16:14 local time, respectively. In the following, data influenced by heavy precipitation, sea ice, or land masses are excluded in the analysis by applying provided data flags. Pixels with light rain, however, are included.

5.1.2 Direct Overpass Analysis

To illustrate the possibility of directly comparing SSMIS to airborne measurements, an example from research flight RF05, 15.12.2013, will be discussed in this section. The example took place between 20:24 and 20:48 UTC, 16:24 to 16:48 in local time, with the respective SSMIS swath measured at 20:36 UTC (16:36 local time). Figure 5.1

shows HALO's flight route and the IWV and LWP from the SSMIS descending evening orbit. From the contours, the different scales of variations can be seen, with LWP varying on a smaller spatial scale than IWV. Starting and ending at Barbados Grantley Adams airport, HALO took the same route eastwards as well as westwards, and was flying westwards during the SSMIS overpass.

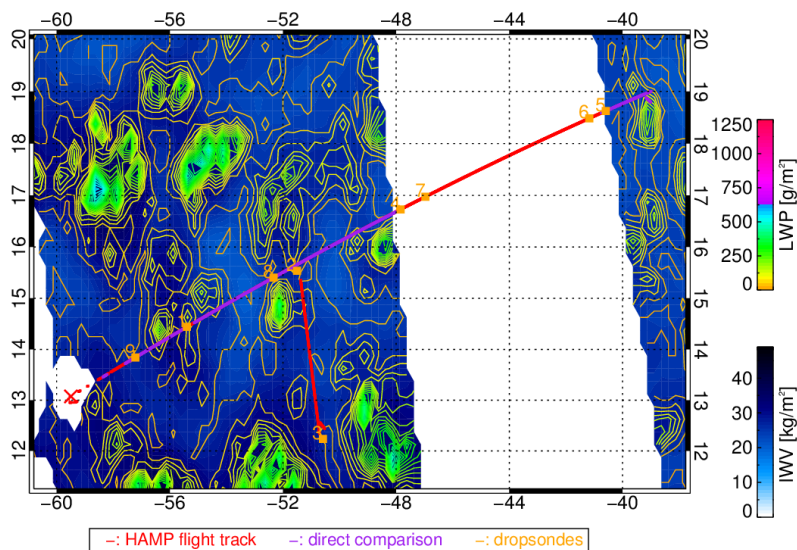


Figure 5.1 – Map of the descending SSMIS swath, 15.12.2015, 20:36 UTC. The IWV distribution is illustrated in blue contours, the LWP distribution is overplotted in lines (yellow to green). Barbados is marked as a red cross. The HALO flight route is shown in red. Coincident measurements with not more of one hour difference are shown in purple. The positions of the launched dropsondes are marked in orange.

A direct comparison between the LWP and IWV of the two sensors is possible at 20:36 UTC and depicted in figure 5.2. For direct comparison, the HAMP product was averaged on the SSMIS pixel size, leading to a value expected if both instruments had the same resolution.

The averaged IWV products match within the associated product uncertainties, representing changes on the 0.25° scale well. In times where the overpassing SSMIS and HAMP measured simultaneously the same scene, SSMIS seems to slightly overestimate the amount of IWV measured by HAMP. In case SSMIS overpassed 7 minutes later (negative time difference area), the IWV captured by SSMIS is smaller than HAMP's observation, which may be associated to decreasing IWV in the atmosphere within this time period between the observations. Even though SSMIS and HAMP agree within their uncertainties, SSMIS cannot capture small scale IWV variabilities in the order of magnitude of less than 3 kgm^{-2} due to the

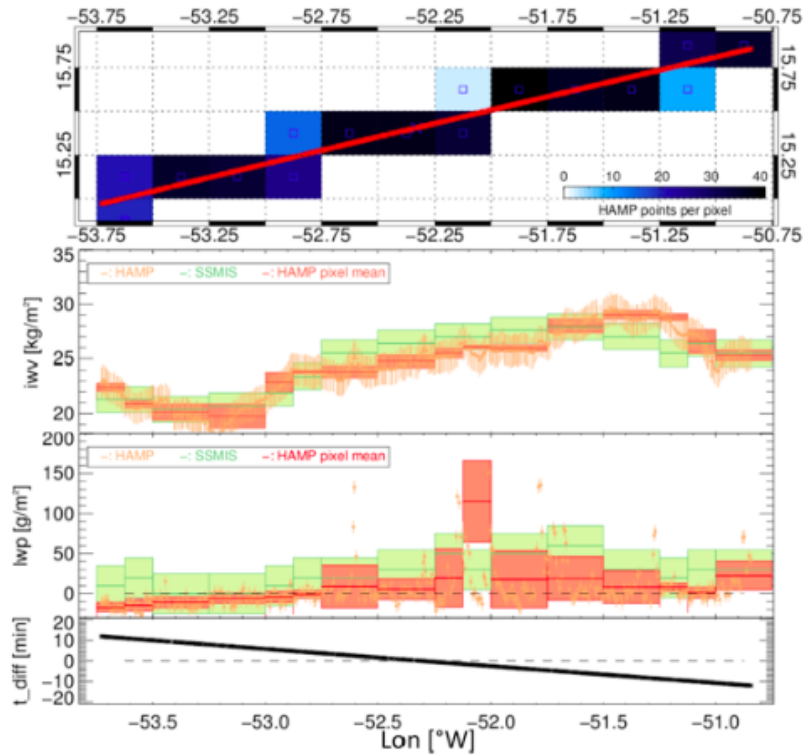


Figure 5.2 – Coincident measurement comparison of HAMP and SSMIS derived IWV and LWP as a function of longitude, observed during RF05, 15.12.2013, 20:24 - 20:48 UTC. The upper panel illustrates the HAMP flight route (red), with the corresponding SSMIS pixels depicted in a different color corresponding to the number of HAMP measurements within each pixel. The middle panels show the HAMP retrieved IWV and LWP (orange) with their associated uncertainty, as well as the pixel means of HAMP (red) and SSMIS (green), shaded with its standard deviation. The lowest panel shows the time difference of HAMP to SSMIS. Positive values represent a later measurement by HAMP.

coarse data resolution. However, in this example the variability of the IWV is low and therefore the satellite observations are similar to HAMP’s IWV.

A comparison of the LWP products yields to similar results as were found for the IWV. In the clear scenarios between -53.75°W and -52.75°W , where LWP variability is within the detection limit of HAMP, the products match within their uncertainties. In cases where the time difference between the two sensors is smaller than 5 minutes, the averaged products show discrepancies when clouds are detected. Single clouds captured by HAMP are completely missed by SSMIS, even though the pixel mean values agree within the assigned errors. Thus, the high LWP variability of up to $50 - 100 \text{ gm}^{-2}$ within one SSMIS pixel cannot be captured by SSMIS due to its coarse resolution.

Direct overpasses occurred in six of the eight flights. Considering all of the cases which occurred with a maximum of one hour time difference, 248 different satellite

pixels can be evaluated to directly compare air- and spaceborne observations. Within all of these coincidentally measured pixels, 6253 HAMP measurements were performed.

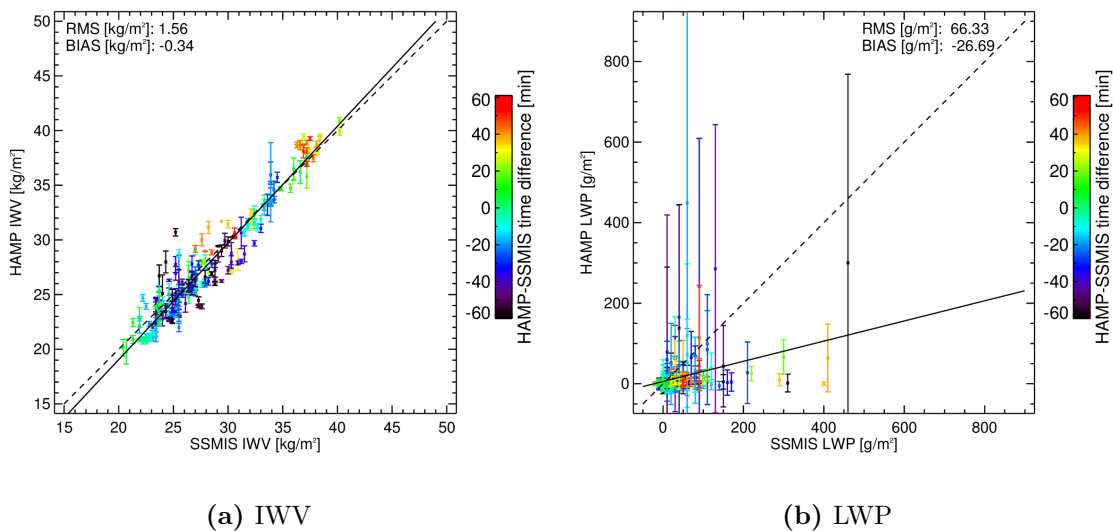


Figure 5.3 – Direct Comparisons of all coincident HAMP airborne and SSMIS spaceborne IWV and LWP retrieval products. Measurements points are colored as a function of time difference. Errorbars represent the standard deviation of the HAMP retrieval product within the measurements’ corresponding SSMIS pixel.

In case of IWV, the result from the case study is confirmed. The variability of IWV can be accurately captured with a spaceborne sensor with a resolution of $0.25^\circ \times 0.25^\circ$, leading to an RMS of 1.56 kg m^{-2} . This RMS is close to the RMS derived from the comparison to measurements by the launched dropsondes (1.40 kg m^{-2}). The bias of -0.34 kg m^{-2} of HAMP to SSMIS values shows a slight overestimation by SSMIS compared to the HAMP values.

However, the statistics of the LWP product disagree more significantly. In this comparison, only LWP values of up to 500 g m^{-2} are included to exclude the occurrence of rain. Clearly, the variability of LWP is not captured by a sensor of a coarse resolution like SSMIS. Referring to the distribution of measured cloud sizes within the campaign derived in section 4.2.2, almost 70 % of the observed clouds were smaller than 2 km in length. The resulting variability of LWP within one satellite pixel can, thus, not be resolved by SSMIS, but is represented by the standard deviations of the HAMP measurements within the pixel.

In situations when HAMP does not capture a cloud, i.e. measures an LWP of 0 g m^{-2} with additional uncertainties, SSMIS captures an LWP of up to 100 g m^{-2} , and,

thus, overestimates the liquid water amount. This is also evident in the significant negative bias of -26.69 gm^{-2} , being the mean difference between HAMP and SSMIS LWP. The RMS was calculated with 66.33 gm^{-2} .

Analysing the differences between the two sensors as a function of time difference between the measurements, it is clearly distinguishable that clouds change on a temporal scale shorter than one hour, as the discrepancy between the captured LWP increases with the time difference (see fig. 5.3b). However, a more time-limited analysis of the data, however, is restricted by the small amount of overpasses, and would reduce the dataset to a statistically insignificant number of observations.

Table 5.1 – Details for comparison between all coincident measurements by HAMP and SSMIS with less than one hour of time difference between the measurements.

	IWV [kgm^{-2}]		LWP [gm^{-2}]	
	HAMP	SSMIS	HAMP	SSMIS
pixels	248		248	
RMS	1.56		66.33	
bias	-0.34		-26.69	
median	26.51	27.00	3.10	30.00
mean	28.22	28.63	62.43	58.87
standard deviation	5.71	5.18	290.27	121.45

Table 5.1 summarises the results from all direct overpass situations. Analysing the medians of the distributions, the overestimation of SSMIS compared to HAMP measurements is also visible. Although the median values only differ by about 2% in the case of IWV, there is a more evident difference in the LWP datasets with the medians disagreeing by 90%. This discrepancy can have two reasons. The negative values in the HAMP retrieval during clear sky scenes introduce a bias in the distribution towards small values. This feature can be removed in further analyses by truncating the data as performed by Horváth and Gentemann [2007]. Secondly, this difference arises due to the coarser SSMIS resolution which cannot represent the spatial LWP variability. This variability is confirmed by the standard deviations of the two datasets, which is 140% higher for the HAMP dataset than for the SSMIS observations.

5.1.3 Regional Distributions

Due to the insufficient availability of direct overpasses, the representativeness of the distributions of directly comparable situations suffers. In a further approach, it will be investigated how the distributions of the air- and spaceborne observations in a tradewind driven region between 300 to 320 °E and 9 to 20 °N change when not applying a time difference threshold to the comparison.

All data from the descending evening orbit and the ascending morning orbit of each of the flight days are investigated, considering only the pixels where HAMP measurements were performed and its eight closest surrounding pixels. Averaging the HAMP measurements within 56 km along the flight route, the resolution of HAMP was down-scaled to the footprint size of SSMIS. In this comparison, only valid data between 0 and 60 kgm⁻² and -100 and 500 gm⁻², respectively, were included, such that the range of all occurring LWP values for non-precipitating clouds is covered. This excluded 4.6 % and 7.7 %, respectively for LWP, of the entire HAMP original dataset, and the flagged 27.0 % of the SSMIS dataset.

For both evening and morning IWV distributions, the original HAMP and averaged HAMP distributions are wider than the corresponding SSMIS distributions. The satellite data distribution covers values between 20 kgm⁻² and 35 kgm⁻² in the evening, and 23 kgm⁻² and 35 kgm⁻² in the morning distribution, respectively. The centers of the two HAMP distributions are located in the bin ranging from 25 to 27 kgm⁻² with about 22 % and 23 % of all considered measurements. The SSMIS evening distribution centers in the same bin with about 40 % of the considered data, whereas the morning maximum is shifted to the next bin ranging from 27 to 29 kgm⁻², representing more than 50 % of the considered data.

Both HAMP LWP distributions center in the bin ranging from -5 gm⁻² to 5 gm⁻², congregating 32 % of the non-averaged and 37 % of the averaged dataset. The averaging leads to the elimination of a small portion of the negative values and an increase in the occurrence of values between 45 and 75 gm⁻². The sawtooth-artefacts occurring above 80 gm⁻² are attributed to the chosen binsize and -locations. The SSMIS distributions are shifted towards more positive values, in the evening orbit with a maximum of 26 % between 15 and 25 gm⁻², re-matching the HAMP distribution in the bin of 55 to 65 gm⁻². LWP measured during the morning overpasses is more widely distributed, re-matching HAMP's measurements between 165 to 175 gm⁻².

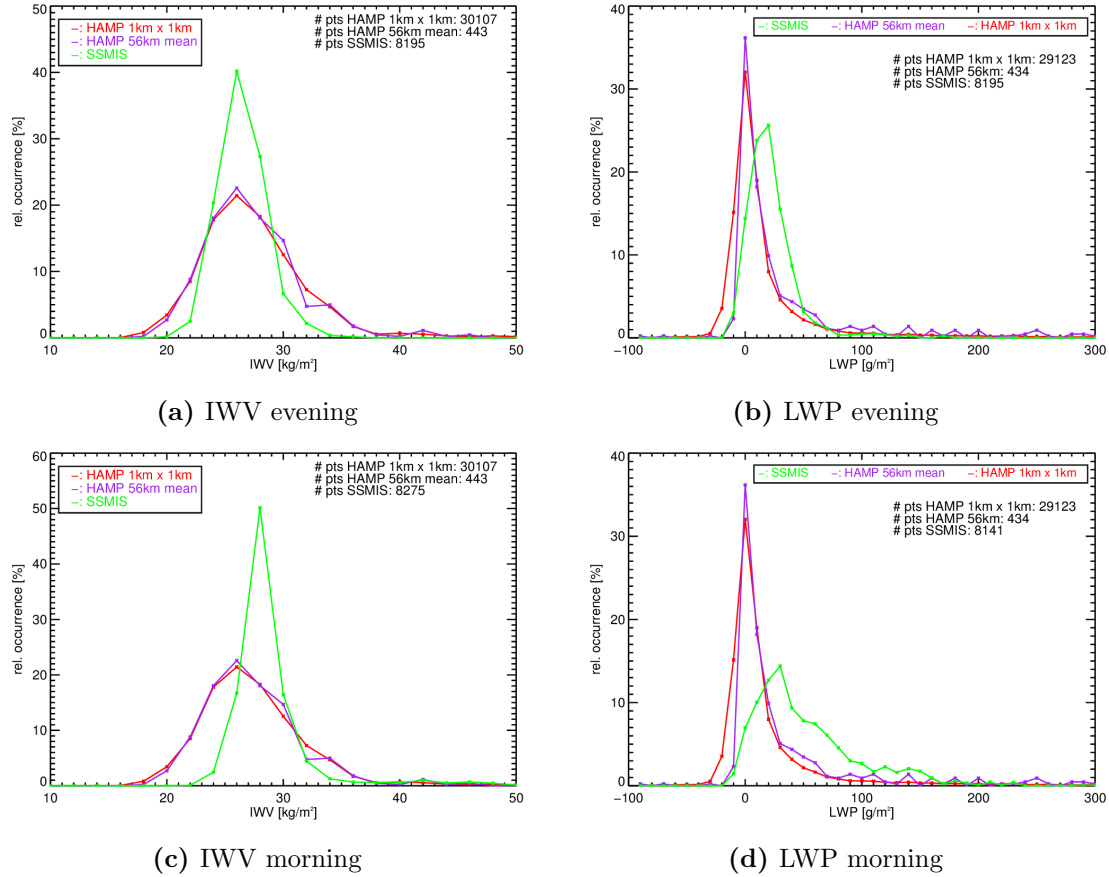


Figure 5.4 – I WV and LWP distribution of all available HAMP data in a resolution of 1km x 1km (red), and averaged over 56 km along the flight track (purple), as well as the respective SSMIS distributions (green). The data are binned to 2 kgm⁻² and 10 gm⁻², occurrences are normalized to all data points lying within 0 and 60 kgm⁻² and -100 and 500 gm⁻², respectively. (a) and (b) show data from SSMIS’s evening orbit overpassing at 16:00 local time, (c) and (d) from the morning orbit at 4:00 local time.

The curve maximum shifted to the bin ranging from 25 to 35 gm⁻², assembling 14% of the analysed data.

The underestimation of LWP below 20 gm⁻² (evening) and 30 gm⁻² (morning) by SSMIS can have two reasons. Due to the footprint size of SSMIS of about 56 km, the probability of a completely cloud-free scene is very low in the tradewind region. Secondly, additional signal originating from the sidelobes of the antenna pattern further increases the probability for LWP larger than 0 gm⁻². As the resolution of HAMP is finer, cases without clouds in the footprint can be resolved. Another reason for the observed discrepancy may be the occurrence of negative values in the airborne retrieval as also seen in section 5.1.2, which can be adapted following the

truncation approach by Horváth and Gentemann [2007], who apply a function to the LWP distribution to up-scale negative LWP to the positive range.

The observed diurnal shifting of the satellite distribution confirms the observations by Wood et al. [2002]. They describe a diurnal cycle of LWP in the Atlantic tradewind region, peaking in the morning around 5:00 local time, which they derived from a 1-year dataset with a resolution of $2.5^\circ \times 2.5^\circ$. The cycle's average amplitude is stated as $\bar{A} = 9.3 \text{ gm}^{-2}$. As the HAMP measurements usually took place between 10:00 and 20:00 local time, this morning maximum of LWP and IWV can only be partially represented in the airborne dataset.

5.2 MODIS LWP

In the following section, the **MOD**erate Resolution **Im**aging **S**pectroradiometer (MODIS) will be introduced, describing the satellite's LWP product in section 5.2.1. A performance example of the direct overpass comparison between MODIS and HAMP will be given in section 5.2.2, leading to a further detailed analysis of all available overpasses during the campaign in section 5.2.3.

5.2.1 Data Description

MODIS, operating from NASA's Aqua and Terra satellites, offers a large variety of Earth observation products by capturing solar reflected radiation in 36 visible or infrared channels with a high resolution of up to 250 m x 250 m (see sec. 2.3). Optical depth τ and the effective radius, r_{eff} are retrieved based on a look-up table approach based on the two-channel retrieval strategy developed by Nakajima and King [1990], implemented for MODIS data by Platnick et al. [2003]. Therein, observed reflectances in the 2.1 μm channel are matched to fit r_{eff} . Over the ocean, the reflectance measured in the non-absorbing 0.86 μm channel is used to find the matching entry in the look-up table for the corresponding τ . If a solution for r_{eff} and τ was found, the resulting LWP for the cloudy pixel is calculated following equation (2.3.2).

The cloud mask algorithm was developed by Ackerman et al. [1998] and improved by Frey et al. [2008] and Ackerman et al. [2008]. Depending on cloud detection tests, i.e. the variation of channel ratios or background signals, the cloud mask algorithm assigns an attribute to each pixel, differentiating between confident clear, probable clear, uncertain cloudy and confident cloudy cases.

Quality parameters help to filter the data, excluding cases when the retrieval failed or was distorted by sun-glint, solid precipitation or land masses. According to Cho et al. [2015], up to 85 % of retrieval failures in the tradewinds are caused by too large retrieved effective radius. Bennartz [2007] found an underestimation of MODIS LWP for vertical inhomogeneous clouds due to the assumption of homogeneous droplet distribution in the cloud and the limited penetration depth of visible and near-infrared radiation into clouds.

MODIS data is provided by Platnick et al. [2015] and is available in different collections. For this study, only data from collection 5.1 was available. The level 2 data with a resolution of 1 km x 1 km is used. Specifically, the atmospheric product

MYD06 containing LWP and the cloud mask, and the corresponding geolocation product MYD03 were downloaded from the MODIS product download website (Platnick et al. [2015]) for all Aqua overpasses during the campaign.

5.2.2 Performance Example

A first case depicting the coincident measurements of HAMP and MODIS was chosen from research flight RF02, Aqua swath at 17:20 UTC. LWP measured by MODIS and the flight route of HALO are illustrated in figure 5.5, resolving the spatial small-scale LWP variations.

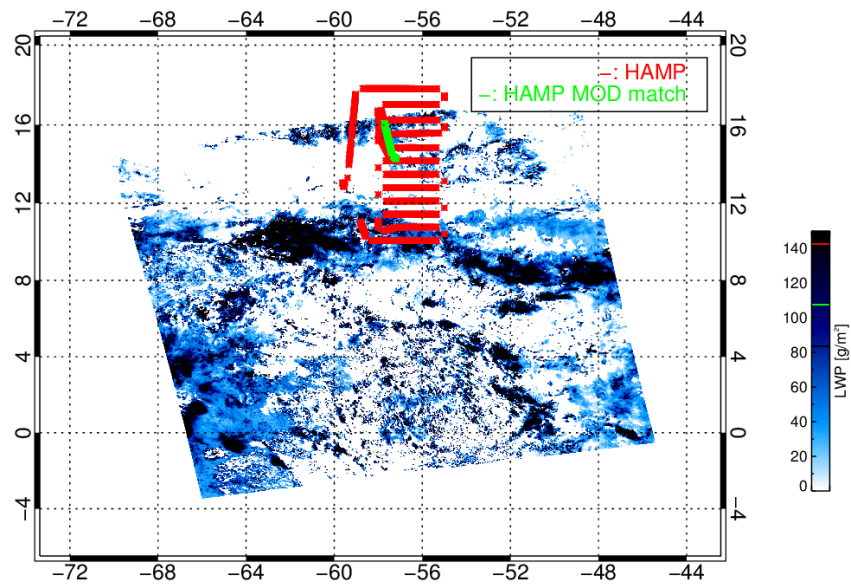


Figure 5.5 – Map of Aqua MODIS swath, 11.12.2013, 17:20 UTC, and flight route of HALO (red). The contours of MODIS LWP show an increase in LWP with darker blue. Coincident measurements with less than 10 minutes time difference are shown in green.

Zooming in on the part of the swath where the time difference between MODIS and HAMP measurements does not exceed 10 minutes, the resulting LWP comparison is shown in figure 5.6.

Excluded points due to quality assurance parameters strongly reduce the number of comparison points by about 70%. In cases where the time difference between the measurements was smaller than 3 minutes, the retrievals show very similar results. However, with increasing time difference, the results show stronger discrepancies, where MODIS seems to miss clouds. This may be due to the fact that in the period

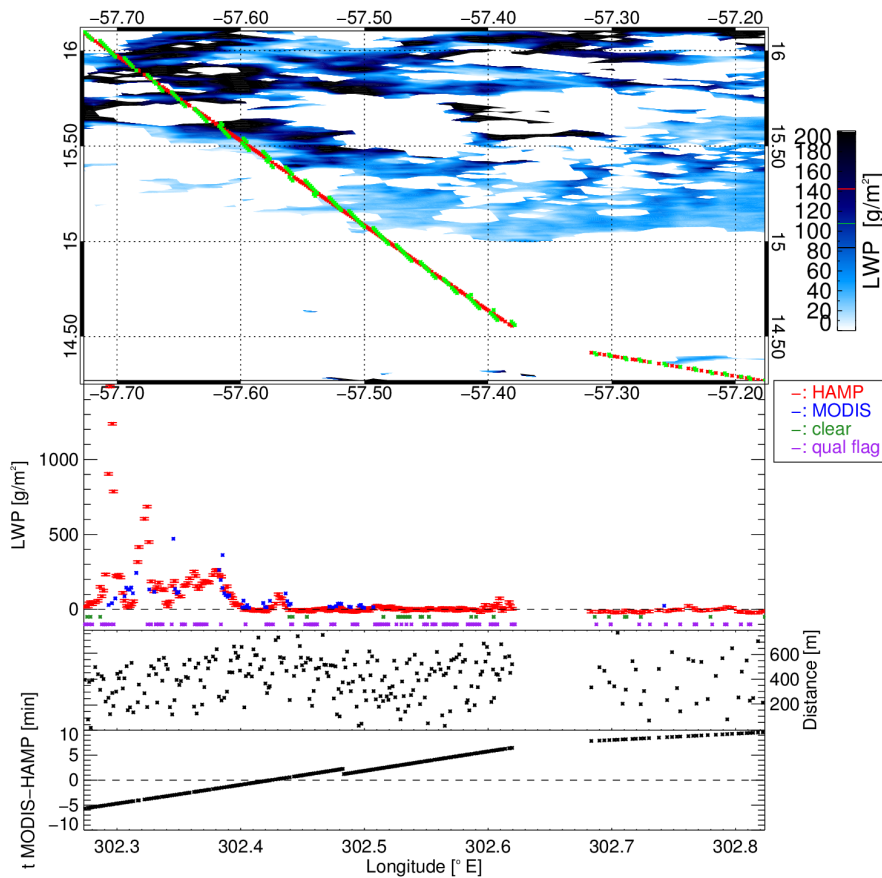


Figure 5.6 – Coincident measurement comparison of HAMP and MODIS derived LWP as a function of longitude, observed during RF02, 11.12.2013, swath of 17:20 UTC between 17:15 UTC and 17:30 UTC. The map in the upper panel shows the MODIS LWP (white-blue scale), the HALO flight route (red), and the nearest MODIS measurements to each HAMP measurement (green). These LWP measurements are compared in the middle panel, showing HAMP LWP with its uncertainty (red), MODIS LWP (blue), as well as cloud mask flagged clear points (green) and quality flagged, excluded, measurements (purple). The two lower panels depict the distance between the center of the MODIS and HAMP footprints and the time difference between the measurements. Positive values mean a later MODIS observation compared to HAMP.

between the measurement times the cloud has dissolved and changed dramatically in LWP, or that MODIS seems to underestimate the amount of LWP due to calculating the LWP from retrieved τ and r_{eff} from cloud top. For the cases where LWP captured by HAMP is larger than 500 gm^{-2} , precipitation might have occurred, biasing the LWP retrieval results.

A second case study measured during a different research flight RF06, 16.12.2013, swath at 16:05 UTC (figure 5.7), provides similar results as the one introduced before.

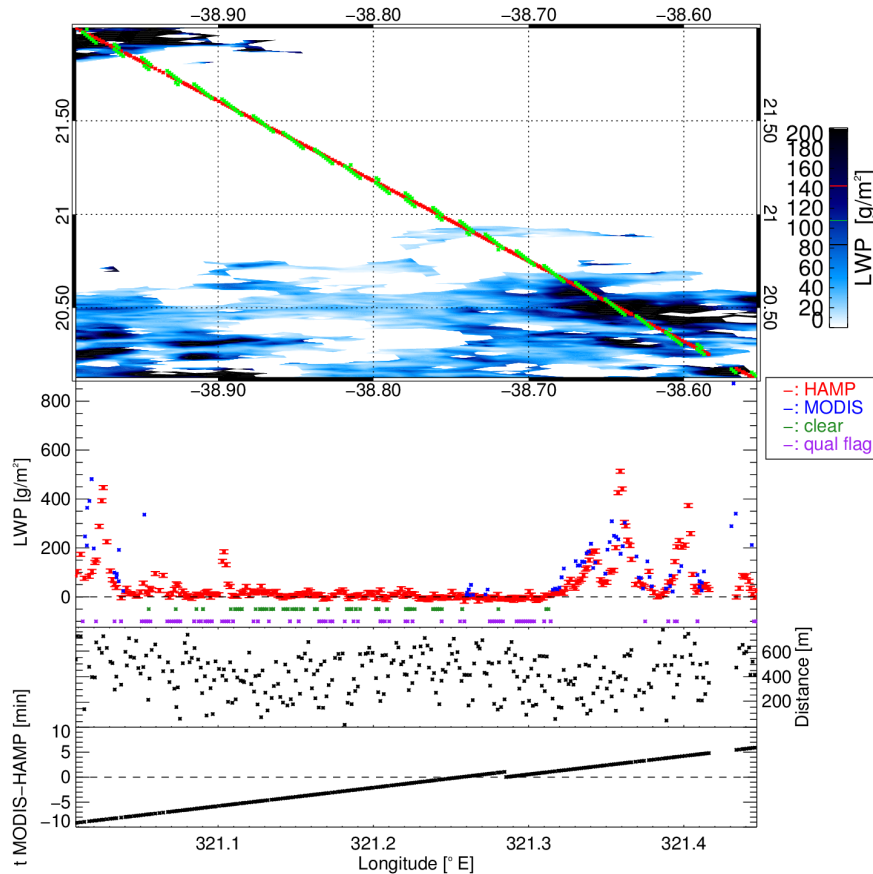


Figure 5.7 – Coincident measurements of HAMP and MODIS LWP as a function of longitude, observed during RF06, 16.12.2013, 16:00 UTC - 16:15 UTC. The map in the upper panel shows the MODIS LWP (white-blue scale), the HALO flight route (red), and the nearest MODIS measurements to each HAMP measurement (green). These LWP measurements are compared in the middle panel, showing HAMP LWP with its uncertainty (red), MODIS LWP (blue), as well as cloud mask flagged clear points (green) and quality flagged, excluded, measurements (purple). The two lower panels depict the distance between the center of the MODIS and HAMP footprints and the time difference between the measurements. Positive values mean a later MODIS observation compared to HAMP.

The observations by both sensors measured at 321.33°E with a time-difference of 2 minutes, show the same LWP results for a cloud with 200 gm^{-2} . One minute later at 321.35°E , with a time difference of 3 minutes, HAMP captured a cloud with an LWP maximum of 550 gm^{-2} , where MODIS only measured 300 gm^{-2} . Considering the radar measurements of this scene (see fig. 5.8), the later cloud had a higher

reflectivity close to cloud center, and a lower cloud base, than the cloud before. The observed LWP difference of 250 gm^{-2} can be attributed to the different properties and retrievals of the sensors. As MODIS LWP is calculated from microphysical properties derived from cloud top, it is not sensitive to larger drops closer to cloud base, which leads to an underestimation of the derived LWP.

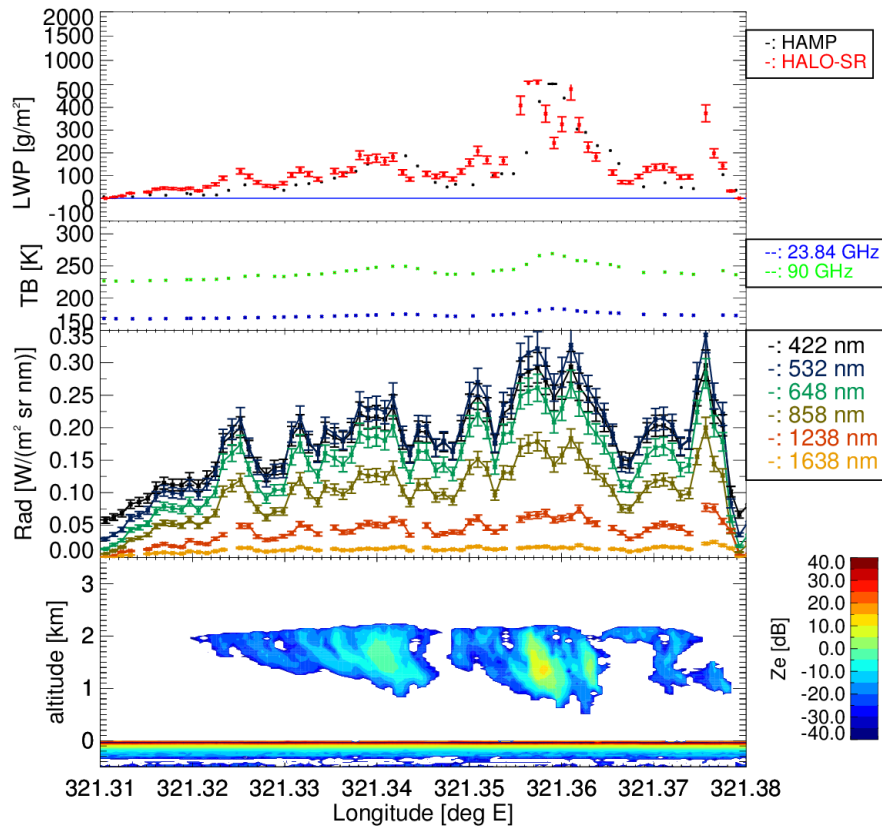


Figure 5.8 – Performance of HAMP active and passive part and coincident HALO-SR radiance measurements, matching the cloud observations at $321.31 - 321.38^\circ\text{E}$ during MODIS overpass, RF06, 16.12.2013, 16:00 UTC - 16:15 UTC. The upper panel shows LWP retrieved from HAMP (black) and HALO-SR (red). The middle panel depicts the measured brightness temperatures of the 23.84 GHz (blue) and 90 GHz-channel (green), as well as the HALO-SR observed radiance in six channels. The radar reflectivity is shown in the lowest panel.

5.2.3 Direct Overpasses Analysis

Direct overpass situations are available from six research flights. As seen in the previous section, the comparison between HAMP and MODIS LWP is very sensitive to the time difference between the datasets as LWP is highly variable on a small temporal and spatial scale.

Considering only measurements which did not exceed a time difference of 10 minutes, the LWP of the almost 800 coincident measurements is shown in a scatterplot, figure 5.9a, with its resulting distributions (figure 5.9b). LWP from pixels with a cloud mask attribute of confident or probable clear were set to 0 gm^{-2} as these values are excluded in the LWP dataset. Again, for precipitation exclusion, only measurements with up to 500 gm^{-2} are included in the analysis to exclude scattering effects of raindrops.

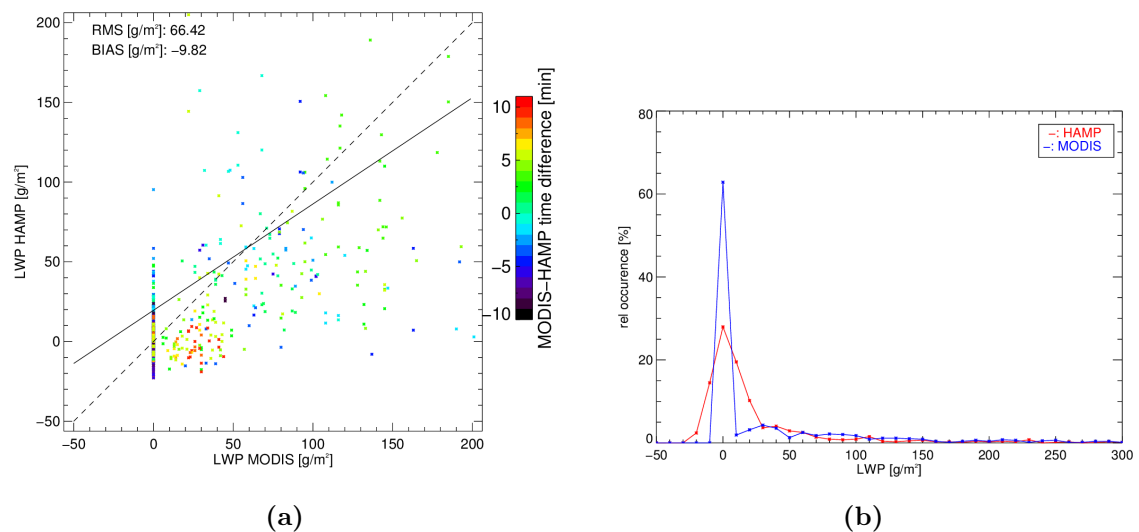


Figure 5.9 – HAMP and MODIS LWP (a) comparison and (b) distributions for all direct overpasses with a time difference of less than 10 minutes. The values in the scatterplots are shown in different colors corresponding to the time difference between the measurements.

In MODIS derived clear sky cases, HAMP captured an LWP of up to 40 gm^{-2} which indicates noise in the HAMP signal or missed clouds in the MODIS signal due to cloud mask failure. MODIS shows a general tendency to overestimate small LWP clouds captured by HAMP with up to 150 gm^{-2} , and to underestimate LWP of up to 500 gm^{-2} . The comparison leads to a calculated RMS of 66.42 gm^{-2} with a bias of -9.82 gm^{-2} . As the scatter around the 1:1 line does not significantly increase with

higher time difference between the two sets, the LWP difference between MODIS and HAMP is not because of the time difference between the measurements if it does not exceed 10 minutes.

Borg and Bennartz [2007] revealed different comparison characteristics. Implementing a one-year long comparison between microwave-retrieved LWP from AMSR-E and optically retrieved LWP from MODIS, they found a good agreement of LWP up to 150 gm^{-2} and an underestimation of LWP by MODIS in larger LWP. They found that this underestimation is due to the vertical homogeneity assumption of the effective radius distribution within a cloud, and suggest to replace this approximation by a vertically adiabatic approach as found by Bennartz [2007] and Brenguier et al. [2000].

The observed under- and overestimations by MODIS LWP are also derivable from the two distributions, respectively. The MODIS distribution is narrow since all clearsky points were set to zero. The overestimation of low LWP values by MODIS is visible in the slightly increased occurrence of values in the bins ranging from 60 gm^{-2} to 160 gm^{-2} , and the fairly lower occurrence of MODIS values in the bins with up to 500 gm^{-2} .

The sensitivity of the derived characteristics to the time threshold was investigated by comparing the results of a ten minute time difference threshold to the statistics when measurements did not exceed 5 minutes as time difference. This restriction diminished the available points to about 500, leading to the results summarised in table 5.2.

Table 5.2 – Details for comparison between all coincident measurements by HAMP and Aqua MODIS with less than 10 and 5 minutes time difference, respectively.

time difference threshold [min]	5		10	
pixels	516		796	
	LWP [gm^{-2}]		LWP [gm^{-2}]	
RMS	46.35		68.00	
bias	3.45		11.70	
	HAMP	MODIS	HAMP	MODIS
Median	6.38	0.00	7.63	0.00
Mean	27.57	31.02	27.41	39.11
Standard Deviation	67.33	63.74	68.72	77.36

The decrease in time difference threshold from ten to five minutes decreased the RMS by 32 % to 46.4 gm^{-2} . The high decrease of 71 % of the bias shows that the time difference between the air- and spaceborne measurements adds an offset error to the comparison, influencing the mean of the MODIS data to a higher degree than the HAMP airborne measurements. The very similar medians of the two distributions suggest that the variability of the LWP seems to be similarly resolved by both instruments.

6 Conclusion and Outlook

Clouds affect us in our daily lives on a small scale, but largely affect the Earth's climate, radiation budget and hydrological cycle. Yet, their representation in climate sensitivity studies is associated with large uncertainties (Stocker et al. [2013]). A major source of these uncertainties are warm, shallow maritime clouds in the subtropics, the so-called tradewind cumuli (Vial et al. [2013], Bony et al. [2015], Zhang et al. [2005], Bony and Dufresne [2005]). Their inhomogeneous and broken structure leads to increased complexity when parametrising this cloud type (Neggers et al. [2003b]) and demands more observations of cloud properties with high precision (Turner et al. [2007], Sengupta et al. [2003]).

Although satellite observations have contributed immensely to data assimilation, they show significant biases between observations performed in the visible and near-infrared, or microwave range (Lin and Rossow [1994], Borg and Bennartz [2007], Horváth and Gentemann [2007], Seethala and Horváth [2010]). Thus, satellite product evaluation is essential to decrease uncertainties in models and retrievals (Stephens and Kummerow [2007]).

HAMP offers potential for satellite product evaluation and airborne characterisation of cloud and water vapor properties on a finely resolved scale (Mech et al. [2014]). Individual vertical cloud properties and water vapor occurrence can be derived from HAMP's passive radiometer based on a statistical quadratic retrieval approach including SST to account for background emissions. Sensitivity studies revealed that in future studies, the retrieval of SST from the observed brightness temperatures may be possible as the influence on the retrieved parameter is low. The theoretical performance of the retrieval tested with simulated data revealed a theoretical retrieval error of $\Delta_{\text{theo}}\text{IWV} = 0.53 \text{ kg m}^{-2}$ and $\Delta_{\text{theo}}\text{LWP} = 27.47 \text{ gm}^{-2}$.

The amount of IWV above HALO at an average flight altitude of 13km was analysed per flight day using radiosonde ascents from Barbados. The IWV above HALO only contributed with up to 0.5% to the total column IWV. As the errors associated to the radiosonde-derived IWV are assumed to be higher than the IWV above 13km, the retrieved IWV is considered to be representative of the entire column.

Comparing the retrieved IWV to coincident dropsonde measurements, the retrieval performance was evaluated for different channel combinations. The combination of information from all K-band channels and the 90 GHz window channel led to the lowest RMS confirming groundbased observations by Löhnert and Crewell [2003] and was used for further analyses. This comparison revealed an IWV retrieval uncertainty of $\Delta\text{IWV} = 1.4 \text{ kgm}^{-2}$.

A clearsky offset correction algorithm was developed and applied to the LWP retrieval similar to van Meijgaard and Crewell [2005]. The LWP detection limit was derived by calculating the width of the first confidence interval of the Gaussian distributed LWP measurements and led to $\Delta\text{LWP} = 8.1 \text{ gm}^{-2}$. In a case study, the clearsky corrected LWP was compared to coincident LWP observations retrieved from HALO-SR reflectance measurements. This comparison revealed good agreement between the two retrieval methods in shallow, non-precipitating clouds.

The sensor synergy of passive and active HAMP components with coincident measurements by HALO-SR were exploited to improve the characterisation of individual clouds but also to derive cloud statistics. The radar does not catch small clouds with LWP smaller than 100 gm^{-2} due to a sensitivity limitations. However, the increased sensitivity of the backscatter signal to larger drops can be exploited to flag retrieval results if precipitation occurred. In future work, this additional information about the atmospheric state can improve the retrieval performance in rainy cases and further investigate the threshold in cloud-rain partitioning microwave retrievals.

Relying on the enhanced sensitivity of radiance measurements by HALO-SR to cloud edges, a cloud mask algorithm was developed similar to the approach described in Frey et al. [2008]. The algorithm's detection performance can still be improved by deriving thresholds per flight instead of only one global threshold to increase the sensitivity to small clouds. Based on the cloud mask, it will be feasible to determine clearsky cases less uncertain than with the standard deviation approach to improve clearsky offset correction and uncertainty analysis in the LWP retrieval. With a more profound analysis of the IWV gradient around the cloud edges, the occurrence of the so-called twilight zone (see Koren et al. [2007] and Lu et al. [2002]) may be analysed in future work.

Relying on the cloud mask performance, a cloud-length statistics was derived for the 3808 detected clouds. The analysis revealed that about 70 % of the clouds had a length of less than 2 km and 46 % of all clouds contained less than 50 gm^{-2} . The size distribution follows a negative power law with an exponent of $\lambda = 1.72$. This result

lies within the predicted range of $\lambda \approx 2$ (e.g. Wood and Field [2011], Benner and Curry [1998], Zhao and Di Girolamo [2007]), but cannot be directly compared to other observations as it depends on the data resolution and binning. If the number of clouds were higher, λ could be calculated by the "direct-power law" method developed by Zhao and Di Girolamo [2007]. In future work, the obtained length and LWP distribution can serve to evaluate LES model parametrisation similar to the work by Neggers et al. [2003b].

Lastly, coincident measurements performed by satellite-based instruments SSMIS and MODIS with coarser and similar resolution, respectively, were compared to the HAMP derived airborne properties. This study was limited by the number of coincident measurements, leading to uncertainties due to temporal displacements of the observations.

Analysing SSMIS overpasses with a time-difference to the HAMP observations of less than an hour showed matching to the HAMP dataset with an RMS of $\text{RMS} = 1.6 \text{ kgm}^{-2}$, a result comparable to the RMS derived from the comparison of HAMP IWV to dropsonde measurements. The observed bias of -0.3 kgm^{-2} shows a slight overestimation of the HAMP measurements by SSMIS, which could result from the time difference between the observations.

In case of SSMIS derived LWP, the spatial variability of tradewind clouds could not be resolved, leading to an RMS of 66.3 gm^{-2} and a bias of -26.7 gm^{-2} when excluding LWP greater than 500 gm^{-2} . Referring to the horizontal cloud statistics, more than half of the occurring clouds change on a spatial scale of less than 2 km, which explains the discrepancies when comparing to coarser resolution observations. The temporal variability of LWP within less than one hour could not be resolved by SSMIS. Further analyses were restricted by the small amount of available overpass situations during the campaign.

Exploiting the strength of the airborne observations to both characterise individual clouds, but also to derive statistical information on a larger scale, the airborne IWV and LWP distributions were compared to the satellite morning and evening observations in a tradewind typical region. The diurnal cycle observed by Wood et al. [2002] is confirmed by the SSMIS data used in this work. Due to the flight times during the campaign, the HAMP data can only partially cover the cycle variations. In a future campaign the flight times could be adapted in order to fully capture the daily variation of LWP.

Comparing HAMP derived LWP to similar resolved MODIS data, the larger availability of direct overpasses allowed to test the sensitivity to smaller time differences between air- and spaceborne observations. As expected, the datasets showed better matching the closer the observations were in time by decreasing the RMS from 68.0 gm^{-2} to 46.4 gm^{-2} . The high LWP variability impacted the comparison when the time difference was greater than 3 minutes.

Similar to Borg and Bennartz [2007], underestimation by MODIS in cases where LWP was larger than 150 gm^{-2} was found. In contrast to Borg's observations, however, lower LWP clouds were overestimated by MODIS. The uncertainties associated to the MODIS LWP product still need to be carefully analysed in following studies. More comparison studies will be performed using the latest collection 6 data, including investigation studies on the dependency of the matching to cloud fraction. These studies can be stretched to analyse the coincident performance of Aqua's AMSR-E, monitoring the same scenes as MODIS with a coarser spatial resolution which is comparable to SSMIS's.

The airborne measurements performed during the NARVAL-South campaign additionally offer the potential to compare to model performances by e.g. ECMWF. By increasing the number of observations by similar planned follow-up campaigns, it is hoped that these observations will contribute to a more thorough understanding of cloud properties in the tradewinds over the Atlantic.

A HAMP Technical Specifications

The following table A.1 sums up some of HAMP's technical specifications.

Table A.1 – HAMP characteristics, summarised from Mech et al. [2014] and Rose [2009].

band	frequencies [GHz]	bandwidth [GHz]	NeDT [K]	HPBW [°]
K H ₂ O	22.24, 23.04 23.84, 25.44 26.24, 27.84 31.40	0.23	0.2	5.0
V O ₂	50.3, 51.76 52.8, 53.75 54.94, 56.66 58.00	0.23	0.2	3.5
W window	90.00	2	0.4	3.3
F O ₂	118.75 ± 8.5, 118.75 ± 4.2, 118.75 ± 2.3, 118.75 ± 1.4,	0.4	0.6	3.3
G H ₂ O	183.31 ± 12.5, 183.31 ± 7.5 183.31 ± 5.0, 183.31 ± 3.5 183.31 ± 2.5, 183.31 ± 1.5 183.31 ± 0.6	0.2	0.6	2.7

Bibliography

- S. A. Ackerman, K. I. Strabala, W. P. Menzel, R. A. Frey, C. C. Moeller, and L. E. Gumley. Discriminating clear sky from clouds with MODIS. *Journal of Geophysical Research: Atmospheres (1984–2012)*, 103(D24):32141–32157, 1998.
- S. A. Ackerman, R. E. Holz, R. Frey, E. W. Eloranta, B. C. Maddux, and M. McGill. Cloud detection with MODIS. Part II: validation. *Journal of Atmospheric and Oceanic Technology*, 25(7):1073–1086, 2008.
- T. P. Ackerman and G. M. Stokes. The atmospheric radiation measurement program. *Physics Today*, 56(PNNL-SA-37894), 2003.
- S. Arabas, H. Pawlowska, and W. W. Grabowski. Effective radius and droplet spectral width from in-situ aircraft observations in trade-wind cumuli during RICO. *Geophysical Research Letters*, 36(11):L11803, 2009.
- A. Arakawa. The cumulus parameterization problem: Past, present, and future. *Journal of Climate*, 17(13):2493–2525, 2004.
- M. Barrera-Verdejo, S. Crewell, U. Löhnert, E. Orlandi, and L. Di Girolamo. Ground based lidar and microwave radiometry synergy for high vertical resolution absolute humidity profiling. *Atmospheric Measurement Techniques Discussions*, pages 1–29, 2016.
- L. J. Battan. *Radar observation of the atmosphere*. The University of Chicago Press, University of Chicago, 1 edition, 1973.
- R. Bennartz. Global assessment of marine boundary layer cloud droplet number concentration from satellite. *Journal of Geophysical Research: Atmospheres (1984–2012)*, 112(D2), 2007.
- T. C. Benner and J. A. Curry. Characteristics of small tropical cumulus clouds and their impact on the environment. *Journal of Geophysical Research*, 103(D22), 1998.
- A. K. Betts. Trade Cumulus: Observations and Modelling. In R. K. Smith, editor, *The Physics and Parameterization of Moist Atmospheric Convection*, pages 99–126. Springer Netherlands, Dordrecht, 1997.

- S. Bony and J.-L. Dufresne. Marine boundary layer clouds at the heart of tropical cloud feedback uncertainties in climate models. *Geophysical Research Letters*, 32(20):L20806, 2005.
- S. Bony, B. Stevens, D. Frierson, C. Jakob, M. Kageyama, R. Pincus, T. G. Shepherd, S. C. Sherwood, A. P. Siebesma, A. H. Sobel, and others. Clouds, circulation and climate sensitivity. *Nature Geoscience*, 8(4):261–268, 2015.
- L. A. Borg and R. Bennartz. Vertical structure of stratiform marine boundary layer clouds and its impact on cloud albedo. *Geophysical Research Letters*, 34(5):L05807, 2007.
- O. Boucher, D. Randall, P. Artaxo, C. Bretherton, G. Feingold, P. Forster, V.-M. Kerminen, Y. Kondo, H. Liao, U. Lohmann, and others. Clouds and aerosols. In *Climate Change 2013: The physical science basis. Contribution of Working Group I to the Fifth Assessment Report of the Intergovernmental Panel on Climate Change*, pages 571–657. Cambridge University Press, 2013.
- J.-L. Brenguier, H. Pawlowska, L. Schüller, R. Preusker, J. Fischer, and Y. Fouquart. Radiative Properties of Boundary Layer Clouds: Droplet Effective Radius versus Number Concentration. *Journal of the Atmospheric Sciences*, 57(6):803–821, 2000.
- E. V. Browell, S. Ismail, and W. B. Grant. Differential absorption lidar (DIAL) measurements from air and space. *Applied Physics B*, 67(4):399–410, 1998.
- H. Chepfer, S. Bony, D. Winker, M. Chiriaco, J.-L. Dufresne, and G. Sèze. Use of CALIPSO lidar observations to evaluate the cloudiness simulated by a climate model. *Geophysical Research Letters*, 35(15):L15704, 2008.
- H.-M. Cho, Z. Zhang, K. Meyer, M. Lebsock, S. Platnick, A. S. Ackerman, L. Di Girolamo, L. C.-Labonnote, C. Cornet, J. Riedi, and R. E. Holz. Frequency and causes of failed MODIS cloud property retrievals for liquid phase clouds over global oceans. *Journal of Geophysical Research: Atmospheres*, 120(9):2015JD023161, 2015.
- E. Chuvieco and A. Huete. *Fundamentals of satellite remote sensing*. CRC Press Inc., 2009.
- D. Cimini, S. Frank, and G. Visconti. *Integrated ground-based observing systems*. Springer-Verlag, 2010.
- E. E. Clothiaux, T. P. Ackerman, G. G. Mace, K. P. Moran, R. T. Marchand, M. A. Miller, and B. E. Martner. Objective Determination of Cloud Heights and Radar Reflectivities Using a Combination of Active Remote Sensors at the ARM CART

- Sites. *Journal of Applied Meteorology*, 39(5):645–665, 2000.
- S. Crewell and U. Löhnert. Accuracy of cloud liquid water path from ground-based microwave radiometry 2. Sensor accuracy and synergy. *Radio Science*, 38(3):8042, 2003.
- W. Demtröder. *Experimentalphysik 3: Atome, Moleküle und Festkörper*. Springer-Verlag, Berlin, 3. edition, 2000.
- DLR. HALO instrumentation. <http://www.halo.dlr.de/instrumentation/basis.html>, 2006a. accessed 2015-12-06.
- DLR. HALO, the german High Altitude and LOng Range Research Aircraft. <http://www.halo.dlr.de/aircraft/schemes/Slide01.png>, 2006b. accessed 2015-12-05.
- W.E. Esaias, M.R. Abbott, I. Barton, Otis B. Brown, J.W. Campbell, K.L. Carder, D.K. Clark, R.H. Evans, Frank E. Hoge, H.R. Gordon, W.M. Balch, R. Letelier, and P.J. Minnett. An overview of MODIS capabilities for ocean science observations. *IEEE Transactions on Geoscience and Remote Sensing*, 36(4):1250–1265, 1998.
- R. A. Frey, S. A. Ackerman, Y. Liu, K. I. Strabala, H. Zhang, J. R. Key, and X. Wang. Cloud detection with MODIS. Part I: Improvements in the MODIS cloud mask for collection 5. *Journal of Atmospheric and Oceanic Technology*, 25(7):1057–1072, 2008.
- C. Fricke, A. Ehrlich, E. Jäkel, B. Bohn, M. Wirth, and M. Wendisch. Influence of local surface albedo variability and ice crystal shape on passive remote sensing of thin cirrus. *Atmospheric Chemistry and Physics*, 14(4):1943–1958, 2014.
- N. Gaussiat, R. J. Hogan, and A. J. Illingworth. Accurate Liquid water path retrieval from low-cost microwave radiometers using additional information from a lidar ceilometer and operational forecast models. *Journal of Atmospheric Oceanic Technology*, 24(9):1562–1575, 2007.
- T. J. Greenwald. A 2 year comparison of AMSR-E and MODIS cloud liquid water path observations. *Geophysical Research Letters*, 36(20), 2009.
- D. L. Hartmann, M. E. Ockert-Bell, and M. L. Michelsen. The Effect of Cloud Type on Earth’s Energy Balance: Global Analysis. *Journal of Climate*, 5(11):1281–1304, 1992.
- J.P. Hollinger, J.L. Peirce, and G.A. Poe. SSM/I instrument evaluation. *IEEE Transactions on Geoscience and Remote Sensing*, 28(5):781–790, 1990.

- Á. Horváth and C. Gentemann. Cloud-fraction-dependent bias in satellite liquid water path retrievals of shallow, non-precipitating marine clouds. *Geophysical Research Letters*, 34(22), 2007.
- A Huete, K Didan, T Miura, E. P Rodriguez, X Gao, and L. G Ferreira. Overview of the radiometric and biophysical performance of the MODIS vegetation indices. *Remote Sensing of Environment*, 83(1–2):195–213, 2002.
- M. A. Janssen. *Atmospheric Remote Sensing By Microwave Radiometry*, volume 1. John Wiley & Sons, Inc, New York, NY, 1993. ISBN 0-471-62891-3.
- J. H. Jiang, H. Su, C. Zhai, V. S. Perun, A. Del Genio, L S. Nazarenko, L J. Donner, L. Horowitz, C. Seman, J. Cole, and others. Evaluation of cloud and water vapor simulations in CMIP5 climate models using NASA “A-Train” satellite observations. *Journal of Geophysical Research: Atmospheres (1984–2012)*, 117(D14), 2012.
- C. Klepp, F. Ament, S. Bakan, L. Hirsch, and B. Stevens. NARVAL Campaign Report. *Berichte zur Erdsystemforschung, Max-Planck-Institut für Meteorologie*, 164, 2014.
- I. Koren, L. A. Remer, Y. J. Kaufman, Y. Rudich, and J. V. Martins. On the twilight zone between clouds and aerosols. *Geophysical Research Letters*, 34(8), 2007.
- C. Kummerow, W. Barnes, T. Kozu, J. Shiue, and J. Simpson. The tropical rainfall measuring mission (TRMM) sensor package. *Journal of Atmospheric and Oceanic Technology*, 15(3):809–817, 1998.
- A. Lammert and F. Ament. Capabilities and uncertainties of aircraft measurements for the validation of satellite precipitation products—a virtual case study. *Meteorologische Zeitschrift*, 24(5):495–502, 2015.
- B. Lin and W. B. Rossow. Observations of cloud liquid water path over oceans: Optical and microwave remote sensing methods. *Journal of Geophysical Research: Atmospheres (1984–2012)*, 99(D10):20907–20927, 1994.
- M. Lu, J. Wang, A. Freedman, H. H. Jonsson, R. C. Flagan, R. A. McClatchey, and J. H. Seinfeld. Analysis and Numerical Simulation of Humidity Halos around Trade Wind Cumulus Clouds. In *AGU Fall Meeting Abstracts*, volume 1, page 0025, 2002.
- U. Löhnert and S. Crewell. Accuracy of cloud liquid water path from ground-based microwave radiometry 1. Dependency on cloud model statistics. *Radio Science*, 38(3):8041, 2003.

- U. Löhnert, J. H. Schween, C. Acquistapace, K. Ebell, M. Maahn, M. Barrera-Verdejo, A. Hirsikko, B. Bohn, A. Knaps, E. O’connor, and others. JOYCE: Jülich observatory for cloud evolution. *Bulletin of the American Meteorological Society*, 96(7):1157–1174, 2014.
- M. Mech, E. Orlandi, S. Crewell, F. Ament, L. Hirsch, M. Hagen, G. Peters, and B. Stevens. HAMP – the microwave package on the High Altitude and LOng range research aircraft (HALO). *Atmospheric Measurement Techniques*, 7(12):4539–4553, 2014.
- S. Melchionna, M. Bauer, and G. Peters. A new algorithm for the extraction of cloud parameters using multipeak analysis of cloud radar data – First application and preliminary results. *Meteorologische Zeitschrift*, 17(5):613–620, 2008.
- T. Nakajima and M. D. King. Determination of the Optical Thickness and Effective Particle Radius of Clouds from Reflected Solar Radiation Measurements. Part I: Theory. *Journal of the Atmospheric Sciences*, 47(15):1878–1893, 1990.
- T. Nakajima, M. D. King, J. D. Spinhirne, and L. F. Radke. Determination of the Optical Thickness and Effective Particle Radius of Clouds from Reflected Solar Radiation Measurements. Part II: Marine Stratocumulus Observations. *Journal of the Atmospheric Sciences*, 48(5):728–751, 1991.
- C. M. Naud, A. D. Del Genio, M. Bauer, and W. Kovari. Cloud Vertical Distribution across Warm and Cold Fronts in CloudSat–CALIPSO Data and a General Circulation Model. *Journal of Climate*, 23(12):3397–3415, 2010.
- R. A. J. Neggers, P. G. Duynkerke, and S. M. A. Rodts. Shallow cumulus convection: A validation of large-eddy simulation against aircraft and Landsat observations. *Quarterly Journal of the Royal Meteorological Society*, 129(593):2671–2696, 2003a.
- R. A. J. Neggers, H. J. J. Jonker, and A. P. Siebesma. Size Statistics of Cumulus Cloud Populations in Large-Eddy Simulations. *Journal of the Atmospheric Sciences*, 60(8):1060–1074, 2003b.
- L. Nuijens, B. Stevens, and A. P. Siebesma. The Environment of Precipitating Shallow Cumulus Convection. *Journal of the Atmospheric Sciences*, 66(7):1962–1979, 2009.
- C. W. O’Dell, F. J. Wentz, and R. Bennartz. Cloud liquid water path from satellite-based passive microwave observations: A new climatology over the global oceans. *Journal of Climate*, 21(8):1721–1739, 2008.

- C.L. Parkinson. Aqua: an Earth-Observing Satellite mission to examine water and other climate variables. *IEEE Transactions on Geoscience and Remote Sensing*, 41(2):173–183, 2003.
- G. W. Petty. *A first course in atmospheric radiation*. Sundog Publications, Madison, Wisconsin, 1 edition, 2006.
- S. Platnick. Vertical photon transport in cloud remote sensing problems. *Journal of Geophysical Research*, 105(22):919–22, 2000.
- S. Platnick, M. D. King, S. Ackerman, W. P. Menzel, B. Baum, J. C. Riédi, R. Frey, and others. The MODIS cloud products: Algorithms and examples from Terra. *Geoscience and Remote Sensing, IEEE Transactions on*, 41(2):459–473, 2003.
- S. Platnick, S. Ackerman, M. King, P. Menzel, G. Wind, and R. Frey. MODIS Atmosphere L2 Cloud Product (06_L2), 2015. URL <https://ladsweb.nascom.nasa.gov/>. accessed 2015-12-08.
- R. M. Rauber, B. Stevens, H. T. Ochs, C. Knight, B. A. Albrecht, A. M. Blyth, C. W. Fairall, J. B. Jensen, S. G. Lasher-Trapp, O. L. Mayol-Bracero, and others. Rain in shallow cumulus over the ocean: The RICO campaign. *Bulletin of the American Meteorological Society*, 88:1912–1928, 2007.
- R. W. Reynolds, T. M. Smith, C.g Liu, D. B. Chelton, K. S. Casey, and M. G. Schlax. Daily high-resolution-blended analyses for sea surface temperature. *Journal of Climate*, 20(22):5473–5496, 2007.
- W. Roedel. *Physik unserer Umwelt: Die Atmosphäre*. Springer-Verlag, Heidelberg, 3 edition, 2000.
- Th. Rose. HAMP (HALO Microwave Package) Radiometer Systems - System Specific Information, 2009.
- W. B. Rossow and R. A. Schiffer. Advances in Understanding Clouds from ISCCP. *Bulletin of the American Meteorological Society*, 80(11):2261–2287, 1999.
- Y. Sato, S. Nishizawa, H. Yashiro, Y. Miyamoto, Y. Kajikawa, and H. Tomita. Impacts of cloud microphysics on trade wind cumulus: which cloud microphysics processes contribute to the diversity in a large eddy simulation? *Progress in Earth and Planetary Science*, 2(1):23, 2015.
- C. Seethala and Á. Horváth. Global assessment of AMSR-E and MODIS cloud liquid water path retrievals in warm oceanic clouds. *Journal of Geophysical Research: Atmospheres (1984–2012)*, 115(D13), 2010.

- M. Sengupta, E. E. Clothiaux, T. P. Ackerman, S. Kato, and Q. Min. Importance of Accurate Liquid Water Path for Estimation of Solar Radiation in Warm Boundary Layer Clouds: An Observational Study. *Journal of Climate*, 16(18):2997–3009, 2003.
- B. J. Soden and I. M. Held. An Assessment of Climate Feedbacks in Coupled Ocean–Atmosphere Models. *Journal of Climate*, 19(14):3354–3360, 2006.
- G. L. Stephens. *Remote sensing of the lower atmosphere*, volume 515. Oxford University Press New York, 1994.
- G. L. Stephens and C. D. Kummerow. The Remote Sensing of Clouds and Precipitation from Space: A Review. *Journal of the Atmospheric Sciences*, 64(11):3742–3765, 2007.
- G. L. Stephens, D. G. Vane, R. J. Boain, G. G. Mace, K. Sassen, Z. Wang, A. J. Illingworth, E. J. O’Connor, W. B. Rossow, S. L. Durden, S. D. Miller, R. T. Austin, A. Benedetti, C. Mitrescu, and The CloudSat Science Team. The cloudsat mission and the a-train. *Bulletin of the American Meteorological Society*, 83(12):1771–1790, 2002.
- B. Stevens. Atmospheric Moist Convection. *Annual Review of Earth and Planetary Sciences*, 33(1):605–643, 2005.
- B. Stevens, D. Farrell, L. Hirsch, F. Jansen, L. Nuijens, I. Serikov, B. Brüggemann, M. Forde, H. Linné, K. Lonitz, and J. M. Prospero. The Barbados Cloud Observatory — anchoring investigations of clouds and circulation on the edge of the ITCZ. *Bulletin of the American Meteorological Society*, 2015.
- T. F. Stocker, D. Qin, G. K. Plattner, M. Tignor, S. K. Allen, J. Boschung, A. Nauels, Y. Xia, B. Bex, and B. M. Midgley. *IPCC, 2013: Climate change 2013: The physical science basis. Contribution of working group I to the fifth assessment report of the Intergovernmental Panel on Climate Change*. Cambridge University Press, Cambridge, United Kingdom and New York, NY, USA, 2013.
- C. J. Stubenrauch, W. B. Rossow, S. Kinne, S. Ackerman, G. Cesana, H. Chepfer, L. Di Girolamo, B. Getzewich, A. Guignard, A. Heidinger, B. C. Maddux, W. P. Menzel, P. Minnis, C. Pearl, S. Platnick, C. Poulsen, J. Riedi, S. Sun-Mack, A. Walther, D. Winker, S. Zeng, and G. Zhao. Assessment of Global Cloud Datasets from Satellites: Project and Database Initiated by the GEWEX Radiation Panel. *Bulletin of the American Meteorological Society*, 94(7):1031–1049, 2013.

- A. M. Tompkins. A prognostic parameterization for the subgrid-scale variability of water vapor and clouds in large-scale models and its use to diagnose cloud cover. *Journal of the Atmospheric Sciences*, 59(12):1917–1942, 2002.
- K. E. Trenberth, J. Fasullo, and L. Smith. Trends and variability in column-integrated atmospheric water vapor. *Climate Dynamics*, 24(7-8):741–758, 2005.
- D. D. Turner, A. M. Vogelmann, K. Johnson, M. Miller, R. T. Austin, J. C. Barnard, C. Flynn, C. Long, S. A. McFarlane, K. Cady-Pereira, S. A. Clough, J. C. Chiu, M. M. Khaiyer, J. Liljegren, B. Lin, P. Minnis, A. Marshak, S. Y. Matrosov, Q. Min, W. O’Hirok, Z. Wang, and W. Wiscombe. Thin Liquid Water Clouds: Their Importance and Our Challenge. *Bulletin of the American Meteorological Society*, 88(2):177–190, 2007.
- F. T. Ulaby, R. K. Moore, and A. K. Fung. *Microwave Remote Sensing: Microwave remote sensing fundamentals and radiometry*, volume 1. Addison-Wesley Publishing Company, Advanced Book Program/World Science Division, 1981.
- E. van Meijgaard and S. Crewell. Comparison of model predicted liquid water path with ground-based measurements during CLIWA-NET. *Atmospheric Research*, 75(3):201–226, 2005.
- J. Vial, J.-L. Dufresne, and S. Bony. On the interpretation of inter-model spread in CMIP5 climate sensitivity estimates. *Climate Dynamics*, 41(11-12):3339–3362, 2013.
- F. Weidner, H. Bösch, H. Bovensmann, J. P. Burrows, A. Butz, C. Camy-Peyret, M. Dorf, K. Gerilowski, W. Gurlit, U. Platt, C. von Friedeburg, T. Wagner, and K. Pfeilsticker. Balloon-borne Limb profiling of UV/vis skylight radiances, O₃, NO₂ and BrO: technical set-up and validation of the method. *Atmospheric Chemistry and Physics Discussions*, 4(6):7631–7665, 2004.
- F. J. Wentz. A well-calibrated ocean algorithm for special sensor microwave / imager. *Journal of Geophysical Research: Oceans*, 102(C4):8703–8718, 1997.
- F. J. Wentz and R. W. Spencer. SSM/I Rain Retrievals within a Unified All-Weather Ocean Algorithm. *Journal of the Atmospheric Sciences*, 55(9):1613–1627, 1998.
- F. J. Wentz, L. Ricciardulli, K. Hilburn, and C. Mears. How Much More Rain Will Global Warming Bring? *Science*, 317(5835):233–235, 2007.
- F. J. Wentz, K. Hilburn, and D. K. Smith. RSS SSMIS Ocean Product Grids Daily from DMSP F16 netCDF. 2012. doi: <http://dx.doi.org/10.5067/MEASURES/>

- DMSP-F16/SSMIS/DATA301.
- E. R. Westwater. The accuracy of water vapor and cloud liquid determination by dual-frequency ground-based microwave radiometry. *Radio Science*, 13(4):677–685, 1978.
- B. A. Wielicki and L. Parker. On the determination of cloud cover from satellite sensors: The effect of sensor spatial resolution. *Journal of Geophysical Research: Atmospheres (1984–2012)*, 97(D12):12799–12823, 1992.
- B. A. Wielicki and R. M. Welch. Cumulus cloud properties derived using landsat satellite data. *Journal of Climate and Applied Meteorology*, 25(3):261–276, 1986.
- M. Wirth, A. Fix, P. Mahnke, H. Schwarzer, F. Schrandt, and G. Ehret. The airborne multi-wavelength water vapor differential absorption lidar WALES: system design and performance. *Applied Physics B*, 96(1):201–213, 2009.
- R. Wood and P. R. Field. The Distribution of Cloud Horizontal Sizes. *Journal of Climate*, 24(18):4800–4816, 2011.
- R. Wood, C. S. Bretherton, and D. L. Hartmann. Diurnal cycle of liquid water path over the subtropical and tropical oceans. *Geophysical Research Letters*, 29(23):7–1, 2002.
- M. H. Zhang, W. Y. Lin, S. A. Klein, J. T. Bacmeister, S. Bony, R. T. Cederwall, A. D. Del Genio, J. J. Hack, N. G. Loeb, U. Lohmann, and others. Comparing clouds and their seasonal variations in 10 atmospheric general circulation models with satellite measurements. *Journal of Geophysical Research: Atmospheres (1984–2012)*, 110(D15), 2005.
- G. Zhao and L. Di Girolamo. Statistics on the macrophysical properties of trade wind cumuli over the tropical western Atlantic. *Journal of Geophysical Research*, 112(D10), 2007.
- P. Zuidema, E. R. Westwater, C. Fairall, and D. Hazen. Ship-based liquid water path estimates in marine stratocumulus. *Journal of Geophysical Research: Atmospheres (1984–2012)*, 110(D20), 2005.

Acknowledgements

Fr. Crewell, thank you for the supervision, discussions, and advice throughout the last year.

Hr. Schlemmer, thank you for making this thesis possible.

Mario and Emiliano - thank you so for all those answered questions, support, and fruitful feedback!!

Dear AG Crewell: thanks for cake, laughter and good times.

Nils, Daphne, Maria - without you, this thesis would have been full with long sentences.

To the WG: you made my time in Köln.

Dear coffee and mate tea: thanks for filling my cup.

Dear Julian, Lili and Daphne - thank you for all that moral support.

Dear Eltern: ohne Euch wär das alles nicht drin gewesen.

